Title
Novel Methodology for Measuring Regional Myocardial Efficiency

Journal
IEEE Transactions on Medical Imaging, 40(6)

ISSN
0278-0062

Authors
Gullberg, Grant T
Shrestha, Uttam M
Veress, Alexander I
et al.

Publication Date
2021-06-01

DOI
10.1109/tmi.2021.3065219

Peer reviewed

Published in final edited form as:

IEEE Trans Med Imaging. 2021 June ; 40(6): 1711–1725. doi:10.1109/TMI.2021.3065219.

Novel Methodology for Measuring Regional Myocardial Efficiency

Grant T. Gullberg [Fellow, IEEE],
Department of Radiology at the University of California San Francisco 94143-0946 USA

Uttam M. Shrestha,
Department of Radiology at the University of California San Francisco 94143-0946 USA

Alexander I. Veress,
Department of Mechanical Engineering, University of Washington, Seattle, WA 98195 USA

W. Paul Segars [Senior Member, IEEE],
Department of Radiology, Duke University, Raleigh-Durham, NC 27710 USA

Jing Liu,
Department of Radiology at the University of California San Francisco 94143-0946 USA

Karen Ordovas,
Department of Radiology at the University of California San Francisco 94143-0946, USA. She is now with the Department of Radiology, University of Washington, Seattle, WA 98195 USA

Youngho Seo [Senior Member, IEEE]
Department of Radiology at the University of California San Francisco 94143-0946 USA

Abstract

Our approach differs from the usual global measure of cardiac efficiency by using PET/MRI to measure efficiency of small pieces of cardiac tissue whose limiting size is equal to the spatial resolution of the PET scanner. We initiated a dynamic cardiac PET study immediately prior to the injection of 15.1 mCi of ^{11}C-acetate acquiring data for 25 minutes while simultaneously acquiring MRI cine data. 1) A 3D finite element (FE) biomechanical model of the imaged heart was constructed by utilizing nonrigid deformable image registration to alter the Dassault Systemes FE Living Heart Model (LHM) to fit the geometry in the cardiac MRI cine data. The patient specific FE cardiac model with estimates of stress, strain, and work was transformed into PET/MRI format. 2) A 1-tissue compartment model was used to calculate wash-in (K_1) and the linear portion of the decay in the PET ^{11}C-acetate time activity curve (TAC) was used to calculate the wash-out k_2(mono) rate constant. K_1 was used to calculate blood flow and k_2 (mono) was used to calculate myocardial volume oxygen consumption (MVO_2). 3) Estimates of stress and strain were used to calculate Myocardial Equivalent Minute Work (*MEMW*) and Cardiac Efficiency = $MEMW/MVO_2$ was then calculated for 17 tissue segments of the left ventricle. The global MBF was 0.96 ± 0.15 ml/min/gm and MVO_2 ranged from 8 to 17 ml/100gm/min. Six central slices of the MRI cine data

gtgullberg@lbl.gov.

provided a range of *MEMW* of 0.1 to 0.4 joules/gm/min and a range of Cardiac Efficiency of 6 to 18%.

Keywords

Cardiac efficiency; cardiac work; cardiac oxygen utilization; finite element electro-mechanical model; MRI; PET

I. Introduction

HEART failure (HF) is the fastest growing clinical cardiac disease that affects over 5 million people, results in over 277,000 deaths per year, accounting for 34% of deaths related to cardiovascular disease, and represents almost 2% of all health care expenditures in the U.S. [1]. Several conditions including ischemia, infarction, hypertension, chemical malady, diabetes, or genetic disorders can lead to unresolved impairment of the heart, compromising its ability to work as a pump and resulting in HF. For one, arterial hypertension affects 1/3rd of the US adult population, over 50% of elderly people (>65 years) [2], and is the most common cause of left ventricular hypertrophy (LVH). We know from our earlier studies that an imbalance between oxidative metabolism and cardiac function appears to be a key factor of LVH progression [3], [4]. Evidences using positron emission tomography (PET) indicate that a decline in fatty acid (FA) consumption, a relative increase in glucose consumption, and a decrease in oxygen consumption are some of the precursors of heart failure [5]. Human studies using magnetic resonance imaging (MRI) also showed a decrease in cardiac circumferential strain with LVH [6] indicating that mechanical and metabolic effects go hand-in-hand reducing efficiency of the heart in patients with LVH.

It has been shown [7] that a 2% change in the normal 25% efficiency of the heart could differentiate patients with LVH from those with normal hearts. Myocardial efficiency is usually measured as overall heart work (work = stroke volume × pressure) divided by oxygen consumption [8]. Myocardial volume oxygen consumption (MVO_2) is the rate at which oxygen is used by myocardial tissues for aerobic metabolism producing CO_2. MVO_2 is usually given in ml of oxygen consumed per 100 grams of tissue per minute which can be related to energy assuming 1 ml oxygen = 21 joules. PET imaging using ^{11}C-acetate as a surrogate for energy input can be used to measure MVO_2 [7]–[15]. ^{11}C-acetate is rapidly picked-up by cardiac cells, metabolized into acetyl-CoA, and enters the tricarboxylic acid (TCA) cycle producing CO_2 and reducing NAD_+ to NADH and FAD to $FADH_2$. The NADH and $FADH_2$ generated by the TCA cycle move into the oxidative phosphorylation pathway consuming O_2 and producing ATP and H_2O. Since the production of $^{11}CO_2$ in the TCA cycle is closely associated with the consumption of O_2 in the oxidative phosphorylation pathway, the oxidation of ^{11}C-acetate is an excellent probe for assessing oxygen consumption by measuring the rate of efflux from the heart tissue of $^{11}CO_2$.

Overall assessment of cardiac work is relatively straightforward by estimating the area contained within the pressure volume-loop (PV-loop) though some methods can be invasive [16]. In this method only knowledge of stroke volume (SV) and end-systolic left ventricular pressure is required. In order to determine efficiency, measures of oxygen consumption by

^{11}C-acetate PET are then combined with measures of cardiac work and arterial pressure to define an overall work-metabolic index [11]. Our approach differs from this global measure in that we seek to measure efficiency of tissue regions whose size is only limited by the resolution of the PET scanner. Regional cardiac tissue efficiency can be obtained by using finite element (FE) cardiac mechanical models to measure Work (stress × strain) accomplished by a volume of tissue divided by the chemical energy expended by the tissue volume measured by MVO_2 using a ^{11}C-acetate radiotracer. Our goal is to provide regional myocardial tissue maps of efficiency rather than global estimates. The regional change in tissue energy efficiency and perfusion are potential new biomarkers that allow identification of regional abnormalities in patients with heart failure, which could perhaps be missed when utilizing only a global approach.

Our work is the first to use nonlinear biomechanics [17]–[29] with data from simultaneous PET/MRI to obtain region by region estimates of cardiac efficiency. PET imaging of ^{11}C-acetate [7]–[15] provides regional MVO_2, whereas MRI provides input to a patient specific FE mechanical model. With an estimate of intraventricular pressure [23] and a nonlinear FE mechanical model [24], [25] as input, Abaqus [26] provides regional estimates of stress and strain to provide measures of external work per tissue regions. The ratio of work to the energy equivalent of oxygen consumption measured by PET gives cardiac efficiency for a unit of cardiac tissue.

A normal heart is approximately 20-25% efficient as measured by the ratio of global external work vs. oxygen consumption with 80-75% lost as heat with the majority of metabolic substrate energy and oxygen consumption needed for electrophysiology and cell maintenance in support of contracting myocytes [30]. The human myocardium at rest uses 8-10 ml O_2 per 100 g per minute and has complete turnover of the ATP pool every 10 secs [6]. In a normal heart this requires oxygen for metabolism of FA as the primary metabolic substrate, accounting for 50-70% of ATP production from FA β-oxidation. FA provides 9 kcal/gram compared to 4 kcal/gram for glucose. This production of ATP is used in several mechanical and non-mechanical functions during the process of active contraction and relaxation including transport of K^+, Na^+, and Ca^{++} across the cell membrane to maintain intra- and extra-cellular concentration and electrical potential differences and the sequestering of Ca^{++} from the cytoplasm into sarcoplasmic reticulum after depolarization. The release of Ca^{++} from the sarcoplasmic reticulum triggers conversion of chemical energy into mechanical work as shown in Fig. 1 through contraction between the thin and thick myofilaments.

This paper provides a methodology for estimating regional myocardial maps of tissue efficiency. This allows for the determination of efficiency heterogeneity related to different cardiac diseases and for the evaluation of the heterogeneity in response to therapeutic interventions. In the following we first describe methods used to process cine MRI data to develop a patient specific FE mechanical model for measuring work in cardiac tissue regions and to process the PET acquired ^{11}C-acetate data to obtain an estimate of MVO_2 in the same cardiac tissue regions as measured by $^{11}CO_2$ efflux from the heart. Results are presented followed by a discussion of potential efficacy of measuring the heterogeneity of cardiac efficiency in cardiac diseases.

II. Virtual Work

If one considers a piece of cardiac tissue that deforms as the heart transforms from end-diastole (ED) to end-systole (ES) or vice versa, the piece of tissue will deform, as measured by strain (dimensionless), experiencing mechanical stress (force per unit area). The forces exerted on the piece of tissue will perform work which depends on the nature of the strains and stresses experienced by the tissue during the deformation. The goal is to measure these strains and stresses to obtain a measure of work performed on individual pieces of cardiac tissue.

The following provides a mathematical representation in Lagrangian curvilinear coordinates (Fig. 2) of the deformation of a volume of tissue. The goal here is to obtain an expression for the strain tensor in terms of the deformed coordinates. The mathematics follows closely the notation in [31]. Extra steps are presented in the Appendix to fill in the gaps between the equations presented in the book [31].

A. Lagrangian Curvilinear Coordinates

A general Lagrangian non-Cartesian curvilinear coordinate system is shown in Fig. 2 for the undeformed state and its convected coordinates for the deformed state. The tangent vectors ($\boldsymbol{g}_1, \boldsymbol{g}_2, \boldsymbol{g}_3$), which may not be orthogonal, are tangent to the initial undeformed curvilinear coordinates ξ_i. Note that the covariant tangent vector $\boldsymbol{g}_i$ is the rate of change (derivative) of $\boldsymbol{r}$ with respect to the curvilinear coordinates ξ_i and $\boldsymbol{G}_i$ is the rate of change of $\boldsymbol{R}$ with respect to the convected coordinates ξ^i:

$$\boldsymbol{g}_i = \frac{\partial \boldsymbol{r}}{\partial \xi_i} = \frac{\partial z_m}{\partial \xi_i} \boldsymbol{i}_m,$$

$$\boldsymbol{G}_i = \frac{\partial \boldsymbol{R}}{\partial \xi^i} = \frac{\partial}{\partial \xi^i}(\mathbf{r} + \boldsymbol{u}),$$

where

$$\boldsymbol{i}_p = \frac{\partial \xi_i}{\partial z_p} \boldsymbol{g}_i = \frac{\partial z_p}{\partial \xi_k} \boldsymbol{g}^k,$$

and the contravariant vector

$$\boldsymbol{g}^i = \frac{\partial \xi_i}{\partial z_m} \boldsymbol{i}_m .$$

Note: $\boldsymbol{g}_i \cdot \boldsymbol{g}^j = \frac{\partial z_m}{\partial \xi_i} \boldsymbol{i}_m \cdot \frac{\partial \xi_j}{\partial z_n} \boldsymbol{i}_n = \delta_{ij}$.

The contravariant vectors $\boldsymbol{g}^1$, $\boldsymbol{g}^2$, $\boldsymbol{g}^3$ are constructed with $\boldsymbol{g}^1$ orthogonal to $\boldsymbol{g}_2$ and $\boldsymbol{g}_3$, $\boldsymbol{g}^2$ orthogonal to $\boldsymbol{g}_1$ and $\boldsymbol{g}_3$, and $\boldsymbol{g}^3$ orthogonal to $\boldsymbol{g}_1$ and $\boldsymbol{g}_2$. This implies $\boldsymbol{g}_i \cdot \boldsymbol{g}^j = \partial_{ij}$ or $\frac{\partial z_m}{\partial \xi_i}\frac{\partial \xi_j}{\partial z_m} = \delta_{ij}$.

Now consider the derivative of the covariant tangent vector $\boldsymbol{g}_i$:

$$\frac{\partial \boldsymbol{g}_i}{\partial \xi_j} = \frac{\partial}{\partial \xi_j}\left(\frac{\partial z_m}{\partial \xi_i} i_m\right) = \frac{\partial^2 z_m}{\partial \xi_j \partial \xi_i}\frac{\partial \xi_n}{\partial z_m}\boldsymbol{g}_n = \Gamma^n_{ij}\boldsymbol{g}_n . \tag{1}$$

Here the symbol Γ^n_{ij} is the Christoffel symbol of the second kind. Using (1), it is easy to derive an expression for the derivative of the contravariant tangent vector $\boldsymbol{g}^j$:

$$\begin{aligned} &\frac{\partial}{\partial \xi_i}(\boldsymbol{g}^j \cdot \boldsymbol{g}_k) = \left(\boldsymbol{g}_k \cdot \frac{\partial \boldsymbol{g}^j}{\partial \xi_i} + \boldsymbol{g}^j \cdot \frac{\partial \boldsymbol{g}_k}{\partial \xi_i}\right) = \frac{\partial}{\partial \xi_i}(\delta_{jk}) = 0, \\ &\boldsymbol{g}_k \cdot \frac{\partial \boldsymbol{g}^j}{\partial \xi_i} = -\boldsymbol{g}^j \cdot \frac{\partial \boldsymbol{g}_k}{\partial \xi_i} = -\boldsymbol{g}^j \cdot \Gamma^n_{ki}\boldsymbol{g}_n = -\delta_{jn}\Gamma^n_{ki} = -\Gamma^j_{ki}, \\ &\frac{\partial \boldsymbol{g}^j}{\partial \xi_i} = -\Gamma^j_{ik}\boldsymbol{g}^k . \end{aligned} \tag{2}$$

B. Strain Tensor in the Deformed Lagrangian Curvilinear Coordinates

Our goal is to come up with an expression for the strain tensor γ_{ij} in the equation of the difference between the deformed and undeformed surfaces (a measure of strain):

$$ds^2 - ds_0^2 = d\boldsymbol{R} \cdot d\boldsymbol{R} - d\boldsymbol{r} \cdot d\boldsymbol{r} = 2\gamma_{ij} d\xi^i d\xi^j, \tag{3}$$

First, we write the differential of the position vector $\boldsymbol{r}$ in the undeformed curvilinear coordinates:

$$d\boldsymbol{r} = \frac{\partial \boldsymbol{r}}{\partial \xi_i} d\xi_i = \boldsymbol{g}_i d\xi_i, \tag{4}$$

and the differential of the position vector $\boldsymbol{R}$ in the undeformed curvilinear coordinates:

$$\begin{aligned} d\boldsymbol{R} &= \frac{\partial \boldsymbol{R}}{\partial \xi_i} d\xi_i = \frac{\partial}{\partial \xi_i}(\boldsymbol{r} + \boldsymbol{u}) d\xi_i, \\ &= \left(\boldsymbol{g}_i + \frac{\partial \boldsymbol{u}}{\partial \xi_i}\right) d\xi_i . \end{aligned} \tag{5}$$

Using (2), one can obtain an expression of the partial derivative of the displacement vector $\boldsymbol{u}$ expressed in terms of the contravariant tangent vectors $\boldsymbol{g}^j$:

$$\begin{aligned} \frac{\partial \boldsymbol{u}}{\partial \xi_i} &= \frac{\partial}{\partial \xi_i}(u_j \boldsymbol{g}^j) = \frac{\partial u_j}{\partial \xi_i}\boldsymbol{g}^j + u_j \frac{\partial \boldsymbol{g}^j}{\partial \xi_i}, \\ &= \frac{\partial u_j}{\partial \xi_i}\boldsymbol{g}^j - u_j \Gamma^j_{ik}\boldsymbol{g}^k . \end{aligned} \tag{6}$$

Therefore,

$$d\boldsymbol{R} = \left(\boldsymbol{g}_i + \frac{\partial u_j}{\partial \xi_i}\boldsymbol{g}^j - u_j \Gamma^j_{ik}\boldsymbol{g}^k\right)d\xi_i = (\boldsymbol{g}_i + \boldsymbol{u}_{,i})d\xi_i, \tag{7}$$

where $u_{,i}$ denotes the partial derivative $\frac{\partial \boldsymbol{u}}{\partial \xi_i}$, and $\boldsymbol{g}_i$ and $\boldsymbol{g}^j$ are covariant and contravariant vectors in the undeformed state, respectively.

Substituting expressions for $\boldsymbol{dr}$ in (4) and $\boldsymbol{dR}$ in (7) into (3), we have the following expression for strain:

$$ds^2 - ds_0^2 = (\boldsymbol{g}_i + \boldsymbol{u}_{,i})d\xi_i \cdot (\boldsymbol{g}_j + \boldsymbol{u}_{,j})d\xi_j - \boldsymbol{g}_i d\xi_i \cdot \boldsymbol{g}_j d\xi_j, \tag{8}$$

where

$$\boldsymbol{u}_{,i} = (u_j \boldsymbol{g}^j)_{,i} = \left(u_{j,i}\boldsymbol{g}^j - \Gamma^j_{ik}u_j\boldsymbol{g}^k\right) \tag{9}$$

is expressed in terms of the contravariant tangent vectors $\boldsymbol{g}^j$.

Following the details in the Appendix, one comes up with the following expression for the strain in terms the strain tensor γ_{ij}:

$$ds^2 - ds_0^2 = \gamma_{ij}d\xi^i d\xi^j, \tag{10}$$

where

$$\gamma_{ij} = \frac{1}{2}\left(u_{i|j} + u_{j|i} + u^m_{|i}u_{m|j}\right) \tag{11}$$

is expressed in terms of the covariant derivatives

$$u_{i|j} = u_{i,j} - \Gamma^m_{ij}u_m,$$

$$u^m_{|i} = u^m_{,i} + \Gamma^m_{ik}u^k.$$

The strain tensor is always covariant where coordinate lines ξ_i are expected to convect to contravariant form ξ^i. Therefore, the measure of strain is in terms of contravariant coordinates ξ^i and strain tensor γ_{ij}. Notice also that the strain tensor $\gamma_{ij} = \left(u_{i|j} + u_{j|i} + u^m_{|i}u_{m|j}\right)/2$ is expressed in terms of covariant derivatives of the displacement vectors. The covariant derivative contains the partial derivative plus the change of the tangent vector due to deformation expressed by the Christoffel symbol.

C. Virtual Work Performed by a Small Piece of Tissue

The concept of virtual work is defined in several books on continuum mechanics: [31]–[34]. In our work we assume the existence of an elastic potential W which is invariant with coordinate transformation of the strain tensor γ_{ij} in (11): $W = W(\gamma_{ij})$. A small change in energy δW due to $\delta\gamma_{ij}$ is related as $\delta W = \sigma_{ij}\delta\gamma_{ij}$, where δ denotes the virtual, incremental, or simply small variation. From $W = W(\gamma_{ij})$, we have $\delta W = (\partial W/\partial\gamma_{ij})\delta\gamma_{ij}$. Equating this with $\delta W = \sigma_{ij}\delta\gamma_{ij}$, implies that the stress tensor σ_{ij} satisfies $\sigma_{ij} = (\partial W/\partial\gamma_{ij})$. Therefore, in our work we assume the virtual work performed on a piece of tissue with volume Ω from end-diastole (ED) to end-systole (ES) is

$$W = \int_{\Omega}\int_{ED}^{ES} \sigma_{ij} d\gamma_{ij} d\Omega . \tag{12}$$

We now consider a special set of axes through a point of tissue where the shear strain components vanish. These axes are the principal axes of strain or principal directions. The eigenvalues λ_1, λ_2, λ_3 that are solutions to

$$|\gamma_{ij} - \lambda\delta_{ij}| = 0 \tag{13}$$

are the principal strains and the principal directions are the eigenvectors $\left(n_1^1 n_2^1 n_3^1\right)$, $\left(n_1^2 n_2^2 n_3^2\right)$, $\left(n_1^3 n_2^3 n_3^3\right)$ that are solutions to the following equations $(\gamma_{ij} - \lambda_1\delta_{ij})n_j^1 = 0$, $(\gamma_{ij} - \lambda_2\delta_{ij})n_j^2 = 0$, and $(\gamma_{ij} - \lambda_3\delta_{ij})n_j^3 = 0$. If $\gamma_{min} = min\{\lambda_1, \lambda_2, \lambda_3\}$, then y_{min} is the minor principal strain equal to the minimum of γ_{11}, γ_{22}, γ_{33} for the strain tensor transformed so that all shear strain components are zero. The same methodology applies for determining the major principal stress. We assume that in curvilinear coordinates the stress components are also covariant $\sigma(\boldsymbol{n}) = \sigma_{ij}g^j n^i$. The stress tensor must be covariant form to be based on the contravariant curvilinear tangent vector g^j and the contravariant normal vector n^i. Let σ_{max} be the major principal stress equal to the maximum of σ_{11}, σ_{22}, σ_{33} when all shear stress components are zero.

In our work, for the virtual work expressed in (12) we integrate the major principal stresses and the absolute value of the minor principal strains from diastole to systole:

$$W = \int_{\Omega}\int_{ED}^{ES} \sigma_{\max} d\gamma d\Omega . \tag{14}$$

where $\gamma = |\lambda_{min}|$. During contraction the minimum principal stain is expected to be negative, so we take the absolute value in our calculation of work.

The paper of [35] provided some estimates of strain throughout the left ventricle. Using FE modeling of human hearts, they found the average maximum principal strain in the equatorial region was 0.60, 0.40, 0.47, 0.33 ± 0.07 in the septal, anterior, lateral, and inferior walls, respectively. For a weakly compressible material, in most regions the maximum principal strain was found to vary around 0.40, and the minimum principal strain varied around −0.20 within a range of about 0.07. Additionally, for a highly compressible material

estimated average values of radial, circumferential and longitudinal strains was found to vary around 0.33, −0.07 and −0.13 within a range of about 0.07, respectively. This was in good agreement with tagged MRI measurements of principal strains [36].

To get a feeling for the magnitude of stress values let's express the stress tensor in the curvilinear spherical coordinates

$$\begin{pmatrix} \sigma_{rr} & \sigma_{r\phi} & \sigma_{r\theta} \\ \sigma_{\phi r} & \sigma_{\phi\phi} & \sigma_{\phi\theta} \\ \sigma_{\theta r} & \sigma_{\theta\phi} & \sigma_{\theta\theta} \end{pmatrix}.$$

In the work of [37], estimates of the tensor component $\sigma_{\phi\phi}$ were performed in different finite element mechanical models where the thickness of the left ventricular wall was varied. They estimated that $\sigma_{\phi\phi}$ would obtain a maximum of 1.44 kPa at end-diastole for a thick wall of 15 mm (someone with hypertrophy), 15.63 kPa for a wall of 2.5 mm, and 99.47 kPa for a thin wall of 0.5 mm (someone with dilated cardiac myopathy) (at a maximum endocardial surface pressure at diastole of 4 kPa [0.58 psi]). In other work estimates of stress along the myofibers were obtain from patient specific mechanical models for five subjects [38]. They predicted end-diastolic and end-systolic myofiber stress for normal five subjects would be 2.21 ± 0.58 and 16.54 ± 4.73 kPa, respectively. Even in very early work using geometrical models instead of FE models, the left ventricular end-diastolic circumferential wall stress in 13 normal subjects was found to average 2.6 ± 2 kPa, while peak systolic circumferential wall stress in this group averaged 37.7 ± 12 kPa [39]. (1 kPa = 7.5 mmHg or 0.145 psi and all measurements presented assume an atmospheric pressure surrounding the body is equal to zero.)

III. Methods

A simultaneous PET/MRI cardiac patient study was performed using a PET/MRI 3.0T scanner (GE Healthcare, Milwaukee, WI) at University of California San Francisco (UCSF). The study was approved by the Committee on Human Research (CHR), the Institutional Review Board (IRB) at UCSF. Informed verbal consent was obtained prior to the scan. A dynamic cardiac PET study began immediately prior to the injection of 15.1 mCi of ^{11}C-acetate acquiring data for 25 minutes while simultaneously acquiring MRI data from cine pulse sequences. The MRI data consisted of 20-time frames of short axis views over the cardiac cycle. The 2D cine data were acquired with field of view (FOV) = 40 cm, radio frequency repetition time/echo time (TR/TE) = 3.2/1.1 ms, frequency band width (BW) = ±127 kHz, image matrix = 192 × 192 (2.1 × 2.1 mm spatial resolution), and 16 mm thickness (6 slices per time frame with 8 mm space between slices).

The 59-year-old male patient had normal wall motion and thickening with left ventricular ejection fraction (LVEF) of 44%, end-diastolic volume (EDV) of 106 ml, and heart rate (HR) of 70 bpm. The patient's blood pressure pre-injection of tracer was 140/83 mmHg and post-injection was 136/81 mmHg. The patient's clinical history showed no evidence of ischemia, or necrosis except prehypertension and obstructive sleep apnea that presented to medical attention with increased fatigue, dyspnea on exertion and decreased exercise

tolerance. EKG showed nonspecific T wave abnormality. Patient had undergone a stress-treadmill test with no EKG abnormalities but a reduced LVEF of 44% – a new finding from previous transthoracic echocardiogram one year prior when LVEF was 60%. Patient had no history of hypertension, smoking or hypercholesterolemia, and was not on any medications.

A. First Task in Data Processing: Create a Patient Specific FE Mechanical Model of the Heart

The model of the heart was developed by utilizing deformable image registration to alter the Dassault Systemes FE Living Heart Model (LHM) shown in Fig. 3 to fit the ventricular geometry given in the cardiac MRI cine data. The patient-based FE model was then analyzed using Abaqus [26] to provide regional stresses and strains.

For a more detailed description of the electro-mechanical modeling of the LHM we refer the reader to [24], [25]. Basically, the LHM is an anatomical four-chamber FE electro-mechanical human heart model created from computed tomography and magnetic resonance images. The FE LHM is discretized with 208,561 linear tetrahedral elements, 47,323 nodes, and 189,292 degrees of freedom (47,323 electrical and 141,969 mechanical degrees of freedom). It consists of a muscle fiber structure helically wrapping around the heart consisting of 208,561 discrete fiber and sheet directions ranging from pointing clockwise-upward on the epicardium to pointing clockwise-downward at the endocardium. A unified finite element environment uses governing equations of excitation-contraction coupling to follow the electrical potential and mechanical deformation across a human heart throughout the cardiac cycle.

The continuum model of tissue stress consists of passive and active contributions; and assumes a Holzapfel-type free energy for the passive tissue stress [40] and active muscle driven by changes in the electrical potential. The passive behavior of the Holzapfel and Ogden material model [40] uses standard material properties defined in the LHM. The heart active contraction is created by adding an active stress to the passive stress such that the total stress σ_f in the fiber direction is equal to the active stress σ_{af} plus the passive stress σ_{pf}: $\sigma_f = \sigma_{pf} + \sigma_{af}$. A time varying elastance model [41] is used to define the active contraction stress in the cardiac muscle fiber direction. The active contraction σ_s in the sheet direction is the sum of the passive stress σ_{ps} and a fraction of the active stress $\eta^*\sigma_{af}$ in the fiber direction, where n is a scalar value less than 1.0 and represents the interaction between the adjacent muscle fibers: $\sigma_s = \sigma_{ps} + \eta^*\sigma_{af}$. Complete details of implementation of both the passive and active material models can be found in [24] as well as [25].

The electrical stimulation is modeled using the monodomain version of the FitzHugh-Nagumo equations [42] with electro-mechanical coupling balanced by kinematic equations, boundary conditions, and constitutive equations. Modeling the interplay between electrical excitation and mechanical contraction provides coordinated opening and closing of heart valves that regulate the filling of the chambers, while the interplay of electrical and mechanical fields controls proper ejection of fluid. The computational model provides a continuous transition over time and space through strong and weak forms of the governing equations that handle internal variables with temporal and spatial discretization, and their linearization. The finite element modeling provides throughout the cardiac cycle discrete

estimates of strain and stress over the myocardium from which one can estimate virtual work of individual tissue regions.

1) Segmentation of Cine MRI Data: The first step in creating a FE cardiac model from the cine MRI data was to segment the patient left and right ventricle in each time frame of the six slices (16 mm slice thickness) covering the length of the LV. The epi-and endocardial walls of the ventricles were manually segmented for each slice of each frame using the Image Segment software developed in the Laboratory of Dr. Paul Segars at Duke, University. The Image Segment software is similar to 3D Slicer (www.slicer.org). A segmented slice is shown in Fig. 4 (left).

2) Aligning the Living Heart Model (LHM) With the Patient Segmented MRI Slices: Once the MRI data was segmented, the FE model of the LHM was aligned with the segmented data. (Fig. 4 [right] shows an example after aligning and warping.) To do this, the FE mesh of the LHM in its unloaded state was exported from the FE program Abaqus and imported into Preview. Preview is the preprocessor of FEBio [27] which is a set of software tools for FE analysis which includes Hyperelastic Warping as a component. In Preview, the LHM mesh was scaled, rotated, and translated to initially align its ventricles with those defined within a given time frame from the MRI data. Since the LHM model was in a relaxed state, it was aligned to the mid-diastolic frame of the MRI data. The rigidly aligned LHM mesh was then voxelized at the same resolution of the MR image, setting the left ventricle (LV) and right ventricle (RV) intensities to correspond to those of the segmented image (Fig. 5A).

3) Hyperelastic Warping the LHM to the Segmented MRI Slices: Hyperelastic Warping [28] was used to determine the non-rigid deformations necessary to register the LHM mesh to the segmented MRI images. The warping analysis was conducted using the template image T (aligned, voxelized and intensity equalized LHM in Fig. 5A) and the given target image S (segmented MRI defined at mid-diastole in Fig. 5C). In order to deform the mesh to match the patient image data, a comparison was made between the template image and the particular target image on a voxel-by-voxel basis. So, an initial rigid transformation was performed in aligning the LHM mesh to the segmented MR image then followed by a non-rigid transformation. The initial rigid alignment aids in the hyperelastic warping calculation.

During warping analysis, the template mesh T is deformed to the target image S through application of an image-based force:

$$F_{image}(r,\varphi) = -\lambda\left[(T(r)-S(\varphi))\frac{\partial S(\varphi)}{\partial \varphi}\right], \tag{15}$$

where $\varphi(r) = R = r + u(r)$ is the deformation map, R is the deformed coordinate corresponding to r, $u(r)$ is the displacement field, and λ is a penalty parameter that enforces alignment of the template model with the target image. The magnitude of the forces applied to the template mesh are determined by the local difference in image intensities ($T(r) - S(\varphi)$). The directions of these applied forces are determined by the partial derivative of the

image energy $\partial S(\varphi)/\partial\varphi$. The body forces were applied at every element of the template FE mesh with the largest forces being applied in regions with large differences in local image intensities usually myocardial boundaries. As $\lambda \rightarrow \infty$, the image energy converges to a minimum value. In other words, these overall differences in image intensities were minimized when the template mesh T was aligned with the MRI target S. (See [28] for more details.)

Initially, following the affine transformations, the template outline in blue in Fig. 5C and the target image S show a mismatch. Following the warping analysis, the LHM outlined in blue in Fig. 5D shows a much-improved match to the target MRI slice, yet for this slice there is still some mismatch in the endocardium of the left ventricle. The mesh created by warping the LHM to the patient MRI data is shown in Fig. 6. The registered LHM mesh was then rotated back to its original, physiological orientation and imported back into the Abaqus/CAE (Complete Abaqus Environment) package.

4) Using Abaqus to Analyze the Created LHM Mesh: The human heart is never completely unloaded even in an arrested condition. The heart, like the arteries and veins, has a pre-stress across the thickness of the atria and ventricles that functions to homogenize the loaded stress across the thickness of the tissue [24]. In order to reproduce this pre-stress, the reference geometry is processed using a series of Abaqus based scripts. Upon completion of these scripts, the new geometry model is analyzed for electrical conduction. The mechanical analysis is completed using the electrical conduction results to drive the contraction of the atria and ventricles.

5) Transforming the Results of the Patient Specific FE Cardiac Model Into PET/MRI Format: Next, the results in Abaqus for estimates of stress and strain of the FE model were used to calculate the Myocardial Equivalent Minute Work (*MEMW*) in the left and right ventricles. Using (14) the absolute value of the minor principal strain component of the strain tensor times the major principal stress component of the stress tensor at elemental points of integration were integrated from end-diastole (ED) to end-systole (ES) using the trapezoidal rule. These values were then averaged over volumes of tissue and were then multiplied by the heart rate and divided by the specific mass:

$$MEMW = \frac{HR}{\rho}\int_{\Omega}\int_{ED}^{ES}\sigma_{\max}d\gamma d\Omega \times \left(joules \cdot meter \cdot gram^{-1} \cdot min^{-1}\right) \tag{16}$$

where σ_{max} is the major principal component of the stress tensor, γ is the absolute value of the minor principal component of the strain tensor, and ρ is the tissue specific mass (1.055 gm/cm^3).

Estimates of stress, strain, and work from the patient specific FE cardiac model were then transformed back into the PET/MRI orientation (Fig. 7) using the same transforms as determined in Step 2. This allowed calculation of the oxygen consumption (MVO_2) in a specific tissue region measured by PET to be registered with the tissue region simultaneously acquired by the MRI data.

Five slices of the cardiac model in MRI format near end-systolic phase are shown in Fig. 8. The cardiac slices are color coded for stress. Stress images were determined from the patient specific FE model oriented to the MRI data. Notice the stress appears to be greatest in the septal wall in the second from the top slice.

B. Second Task in Data Processing: Processing Dynamic PET Data

During the time of the MRI data acquisition a cardiac PET study acquired dynamic data for 25 minutes after the injection of 15.1 mCi of ^{11}C-acetate. Three orthogonal views of images of ^{11}C-acetate uptake in Fig. 9 show excellent resolution provided by the time-of-flight PET camera.

The dynamic PET ^{11}C-acetate data were analyzed in PMOD software (PMOD Technologies, Zurich, Switzerland) assuming a simple 1-tissue compartment model to calculate wash-in (K_1) and wash-out (k_2) rate constants for 17 standardized segmented myocardial tissue regions specified by the American Heart Association (AHA). The wash-in rate constant K_1 was used to calculate myocardial blood flow (MBF) [15]. The time activity curves (TACs) were also fitted with mono-exponential functions to estimate the decay constant k_2(mono). The rate constant k_2(mono) was used to calculate the tissue oxygen consumption using the expression

$$MV\ O_2 = 135[k_2(mono)] - 0.96(\text{ml/100gm/min}), \tag{17}$$

where we assumed 1 ml oxygen = 21 joules [13]. The rate constants k_2(mono) correlates well with the rate-pressure product and has been experimentally useful for detection of net myocardial oxygen utilization [9]. We did not correct for the $^{11}CO_2$ contribution in the PET-derived blood activity.

C. Third Task in Data Processing: Calculating Cardiac Tissue Efficiency

Cardiac efficiency was then calculated for 17 standardized segmented myocardial tissue regions specified by the American Heart Association (AHA) by dividing the myocardial equivalent minute work (*MEMW*) in (16) by the $MV\ O_2$ in (17):

$$\text{Cardiac Efficiency} = MEMW / MV\ O_2 . \tag{18}$$

Bull's-eye plots were constructed using MATLAB comparing differences between MBF, $MV\ O_2$, *MEMW*, and Cardiac Efficiency.

IV. Results

A. Mechanical Work

The temporal changes in 21 equally spaced time frames are shown in Fig. 10 of the major principal component of the stress and the absolute value of the minor principal component of the strain tensor from end-diastole to end-systole. Notice the extremely low stress during the diastolic phase of the cardiac cycle. It is also apparent that the strain in the FE model is nonzero even as the heart is loaded with pre-strain before the cardiac cycle begins. The strains are referenced to this nonzero initial state and this serves to homogenize the stresses

across the wall. As expected, the principal components of the stress and strain are higher during systolic phases compared to diastolic phases. Note that the transmural fiber strain is fairly uniform as compared to the stress. The average absolute value of the minor principal strain in the equatorial region was 0.3139, 0.3402, 0.3398 and 0.4056 in the septal, anterior, lateral, and inferior walls, respectively. Contrary to that reported in [29], our work shows an inhomogeneous distribution of transmural fiber stress, where stress is higher in some septal regions and along the epicardium, which may have to do with the patient's underlying health.

Figure 11 shows in six myocardial slices the average absolute value of the minor principal strain, average major principal stress (MPa), and mechanical work (J/g/min) using (16) with a heart rate of 70 bpm.

The myocardium was segmented as shown in Fig. 12 into a clinically relevant 17-segment model from base through midventricle to apical segments. The regional *MEMW* for each segment was calculated by averaging the work values from all voxels in the segmented region of interest (ROI). These values are displayed in a polar map in Fig. 13 using MATLAB.

B. Chemical Energy – Oxygen Utilization (MVO_2)

Images in Fig. 14 of the 17-segmented model in Fig. 12 provide Bull's-eye plots of myocardial blood flow (MBF) along with wash-out rate constants k_2 estimated using a 1-tissue compartment model for ^{11}C-acetate. MBF was fairly homogeneous throughout the myocardium with a slight decrease in the mid-inferior-apical region. The global MBF = 0.96 ± 0.15 ml/min/gm. Since a 1-tissue compartment model overestimates the wash-out rate k_2, the MVO_2 was determined by k_2(mono) that was obtained by fitting the mono-exponential decay in the TAC [9] and using (17). The mean k_2(mono) = 0.099 ± 0.025 min^{-1} and mean oxygen consumption in the total myocardium was MVO_2 = 12.3 ± 3.4 ml/100gm/min, which is consistent with previous findings for a normal heart at rest that consumes approximately 8 to 12 ml/100gm/min determined invasively by the Fick's method [13]. However, it is reasonable to expect an increase in MVO_2 in a hypertensive patient in response to an augmented metabolic demand caused by a higher workload. The normalization of MVO_2 in the failing heart may occur at the later stage of disease progression.

C. Cardiac Tissue Efficiency

Bull's eye plots of the regional distribution of MVO_2, *MEMW*, and Efficiency (*MEMW*/MVO_2) are shown in Fig. 15 and corresponding bar graphs are shown in Fig. 16 for four segments of the myocardium.

The myocardial distribution of MVO_2, *MEMW*, and Efficiency may be heterogeneous despite the patient not having any significant heart disease. This heterogeneity in the contractility of the myocardial tissue may indicate that the energy utilization in different regions of the myocardial wall may vary; for instance, septal wall may be more efficient than the lateral wall.

In summary, we consider a piece of myocardial tissue (size limited to the spatial resolution of the PET scanner) is allowed to deform by the equations we express in Section II. In doing so the piece of tissue will perform work by nature of the strain and stress forces exerted during the process of deformation going from a state at ED to ES. The energy to perform this work involves chemical energy in the production of ATP which is used in the process of active contraction of the myofibers resulting in deformation of the piece of tissue. PET with ^{11}C-acetate is used to measure the amount energy expended to produce ATP. We assume that we can measure this energy at the resolution of the PET scanner by using (17): $MVO_2 = 135[k_2(mono)] - 0.96$(ml/100gm/min), to obtain a measure of oxygen consumption for the piece of tissue and relating this to energy assuming 1 ml oxygen = 21 joules. The work expended by the deformation divided by the energy expended as measured by ^{11}C-acetate provides the measure of efficiency for the piece of tissue. This explanation of quantifying a piece of tissue is important because it differs from the total global cardiac efficiency of the total myocardium as measured by a PV-loop and total oxygen consumption.

V. Discussion

This work is the first to show the feasibility of estimating cardiac tissue efficiency of specific tissue regions in human using a FE mechanical model of segmented MRI images of the heart to calculate work and kinetic modelling of PET dynamic ^{11}C-acetate data to calculate flow and oxygen consumption. Cine MRI data and nonlinear biomechanics are used to obtain a patient specific nonlinear FE mechanical model that uses hyperelastic warping [28] to register the LHM [24], [25] to the segmented short axis MRI slices. The registered model used as input to Abaqus [26] provides regional estimates of strain and stress. Combining this with dynamic PET estimates of oxygen utilization provides a measure of tissue efficiency for specific cardiac regions. using PET and MRI together for calculating, evaluating, and studying myocardial tissue efficiency in patients, provides a wealth of diagnostic information from functional analysis as well as biochemical and physiological characterization of inhomogeneity of cardiac efficiency and relationships between myocardial metabolism, perfusion, structure, and wall dynamics.

Simultaneous PET/MRI is able to reconstruct accurate PET images fused with MRI and provide anatomic and metabolic characterizations of cardiac diseases. PET/MRI has shown to be useful in imaging viability and assessment of inflammatory and infiltrative processes in myocarditis and cardiac sarcoidosis [43]. Assessing inflammation is especially important in characterization of tissue integrity after acute myocardial infarction (AMI) and is possible using MRI T1 and extracellular volume (ECV) mapping as well as ^{18}fluorodeoxyglucose (^{18}FDG) PET imaging targeting inflammatory cell populations [44]. Combining MRI with PET imaging of ^{18}FDG shows promise as a noninvasive approach to gain knowledge of cardiac function in hypertrophic cardiomyopathy relative to substrate utilization [45]. Cardiac PET/MR imaging also has the potential to assess cardiac tumors, ischemia, infarction, and function [46]. In characterizing perfusion defects, it may be that the integration of the differences in myocardial perfusion quantification of simultaneously acquired $^{13}NH_3$ - ammonia PET and dynamic contrast enhanced (DCE) MRI data in patients at rest and stress will be able to better delineate defects and quantify perfusion in extended microvascular disease [47]. PET/MRI can also potentially provide useful biomarkers to

follow therapies related to metabolic manipulations [48] and mesenchymal stem cell induction [49] as treatments for heart failure (HF).

Cardiac tissue efficiency is an important additional measure for evaluating cardiomyopathies because a common feature is the inherent inefficiency of the heart in using oxygen to metabolize energetic substrates for the production of external work. In hypertensive left ventricular hypertrophy decreases in myocardial fatty acid oxidation correlated with decreased myocardial efficiency [7]. In HF cardiac efficiency is impaired because oxygen consumption is elevated for a given amount of work [50]. It has been found that efficiency measures are beneficial in monitoring various therapies, including drug therapies [51], [52], devices [53], and interventions [54], [55]. It has been found that it is important to carefully plan cardiac resynchronization therapy (CRT), because properly done CRT can improve cardiac efficiency by a higher stroke volume index without increase in metabolic cost [56]. Measuring cardiac efficiency is important in understanding the status of the diabetic heart where decreased cardiac efficiency is caused by oxygen waste for noncontractile purposes such as abnormal Ca^{2+} homeostasis that increases MVO_2 and reduces efficiency [57]. Myocardial oxidative metabolism is also disturbed in cardiac amyloidosis patients with increased total MVO_2 and reduced myocardial external efficiency [58]. Measures of myocardial efficiency using PET has been used to evaluate sympathetic reinnervation after orthotopic heart transplantation [59]. The aging heart also shows a decrease in cardiac efficiency [60]. In advanced age, the resting MVO_2 and cardiac work in the rat remain intact; however, cardiac efficiency achieved at high demand are decreased with age, compared to the young.

Our preliminary results using simultaneous microPET/MRI (Fig. 17) showed a negative correlation between work and glucose metabolism indicating that the heart prefers substrates that maximize efficiency such as fatty acids (FA). However, during hypoxic stress an increased LV systolic function is coupled with an increase in myocardial FDG uptake [61]. Correlations between regional cardiac efficiency and flow and metabolic substrate utilization can be determined by using additional measurements: MBF using ^{11}C-acetate [14], [15], myocardial FA utilization using ^{18}FTHA [3], [4], and myocardial glucose metabolism using ^{18}FDG [3], [4], [50].

Cardiac efficiency is usually measured as overall heart work divided by oxygen consumption. Assessment of heart work is estimated from the area contained within the pressure volume-loop (PV-loop). Instrumentation, such as an in vivo pressure volume conductance catheter, can provide accurate measurements of volume and pressure but is invasive [16]. Recently Harms and co-workers [11] described a method of using only PET to obtain a global measure of flow, MVO_2, and mass to obtain a global measure of cardiac efficiency. From a single dynamic ^{11}C-acetate PET scan, their approach was to use the early first pass phase of a dynamic PET scan for determining forward cardiac output (mL min^{-1}) and the peak uptake phase for determining left ventricular mass; and to combine this with systemic blood pressure and wash-out rate of $^{11}CO_2$ as a measure of oxygen consumption, to obtain a global measure of myocardial efficiency. This work was highlighted by Bengel in an editorial in the Journal of Nuclear Cardiology [50] where other previous works [51] using only a dynamic ^{11}C-acetate PET scan combine measures of oxygen consumption with

measures of cardiac output and arterial pressure to obtain an overall measure of cardiac efficiency. Work of de las Fuentes and co-workers [7] used both PET and MRI to obtain a global measure of cardiac efficiency using measures of ^{11}C-acetate with PET to obtain oxygen utilization and a separate MRI study fitting tagged and cine data to a linear mechanical model to obtain measures of work. Our approach differs from these global measures of cardiac efficiency in that we measure efficiency of tissue regions whose size is only limited by the resolution of the PET scanner.

A. Limitations

In addition to developing our methodology and evaluating with only one patient study, there are limitations that arise in attempting to model complex physiological processes involving cardiac function. More work is needed to determine how sensitive the efficiency estimation is related to the accuracy of the cardiac FE mechanical model. The challenge in obtaining patient specific FE cardiac models is in obtaining subject-specific material properties [63], fiber structure, and intraventricular pressures. We are encouraged by an analysis [38] showing FE model results insensitive to variations of intraventricular pressures within normal range. We are also encouraged by our extensive work in validating our previous mechanical models of the heart. In early work [19] using models of normal, subendocardial ischemia, and transmural anterior ischemia, we demonstrated radial, circumferential, and longitudinal strain distributions results consistent with cine and tagged MRI results. In later work [20] we demonstrated how by changing material properties we could reproduce dyskinetic behavior in LV wall motion for regions of myocardial fibrous and remodeled infarctions. The results were consistent with results reported in the literature. We also investigated effects of fiber disarray through simulations of fibers distributed randomly about angles from 3° to 30° [65]. Fiber disarray up to values of 4° exhibited no compromise in the hemodynamic systolic parameters. Disarray values of 10° or greater show ever increasing degradation of systolic function, including lower systolic volumes and lower ejection fractions. Results showed the pronounced effects of disarray upon systolic function, whereas the diastolic function remained largely unchanged. The fiber strain remained unchanged with ever increasing disarray up to 4°, whereas the models above 10° did not contract sufficiently to produce the necessary fiber strains. In contrast, the first principal strain results showed that the wall strain values increased with decreasing systolic function. The extraction of patient specific fiber structure is a challenge; however, recent developments in DTMRI [66] are also encouraging where diffusion images of the heart could be obtained on human subjects in a reasonable time for specifying subject-specific fiber structure [67].

In a later publication [64] we demonstrated the accuracy of warping PET patient data to design a mechanical model by validating the results with tagged MRI data of the same patient. This was different than what we did in the present work where cine MRI data was used to design the cardiac mechanical model using hyperelastic warping. However, the previous work provides insight into the accuracy of warping. In that work the results of deformation by warping PET data gave results of strain that correlated well with MRI tagged data. The qualitative and quantitative evaluations of the validation study indicated that warping analysis of clinical PET images can provide point strain predictions consistent with

those determined by tagged MRI analysis. Specifically, in that work model values were modified to fit the data. Rather than rely on literature values for the active contraction, a subject specific active contraction methodology was developed and applied to globally align the template FE LV model with the end-systolic image by modifying the inherent active contraction properties in the model [17], [18]. The amount of active contraction applied to the models was governed by the amount of intensity mismatch in the images themselves. Thus, any initial mismatch in the initial warping analysis can be fine-tuned by modifying properties of the model. In our present work this was accomplished by using Abaqus to study and compare the dynamic deformation of the resultant model properties, modifying them if necessary, to better fit the imaging data.

These observations were made with models that we had designed in our own lab. With the development of the LHM of a full heart model including electrical modeling, we focused on using the LHM to process our PET/MRI model. This LHM is considerably more complex and precise with material properties, fiber and sheet structure, electrical stimulation, and variable LV pressure feedback with a total peripheral vascular flow model. Even though with this precision, it is pointed out in their publication [24] that there are limitations. In particular, it is difficult to simulate any of the compensatory mechanisms such as the autonomic neuronal response to a failed myocardium. However, we feel our work is based upon the most realistic model of the living human heart that has been developed to date.

There have been several discussions of the appropriate methods to model in vivo kinetics of ^{11}C-acetate [12], [13], [68]–[70]. In an early paper [68] one, two and three-tissue compartment models were compared for modeling the kinetics of ^{11}C-acetate. Another early paper devil more deeply into the biochemical processes deriving analytical equations of a five-compartment model detailing the metabolic pathways of free acetate, activated acetate, $^{11}CO_2$ precursors, amino acids, and $^{11}CO_2$ in the blood and tissue and cellular components [12]. However, when using imaging to model biological processes only a few parameters can be extracted with reasonable accuracy by mathematical estimation, implying only a few model compartments can be identified.

One problem with ^{11}C-acetate is that $^{11}CO_2$ is released from the tissue into the blood. This creates a contamination of ^{11}C not tagged to the ^{11}C-acetate tracer; thus, biases the blood input function due to efflux of $^{11}CO_2$ into the blood. Modification of models have been proposed to correct for the $^{11}CO_2$ contamination in the blood input function. In one [69], a 2-compartment model with tissue recovery coefficient was proposed. In another [70], a one tissue compartment model used an averaged metabolite correction of the input function proposed by [68]. The concentration of $^{11}CO_2$ was expressed as % total ^{11}C concentration and the continuous time course was approximated by an exponential decay function.

In our work the wash-out k_2(mono) of $^{11}CO_2$ was estimated by fitting a mono-exponential decay in the time activity curve. Blood flow was estimated using a one compartment model without any correction for $^{11}CO_2$ in the blood so that the nonlinear estimation problem might have better solvability properties. Thus, our values may be biased upwards. As with any flow tracer there is the need to correct for the flow dependent extraction fraction as was performed internally in our PMOD data processing program. The correction for partial

volume effects can also improve the accuracy [71]. Another aspect to consider is the relation between myocardial clearance kinetics of ^{11}C-acetate, and the rate-pressure product as an index of myocardial flow and oxygen consumption [9].

B. Conclusions

Our method will provide a determination of efficiency heterogeneity related to different cardiac diseases and for evaluating the heterogeneity in response to therapeutic interventions. Data from Fig. 17 would suggest that the heart has a heterogeneity response to work and metabolism. This heterogeneity could provide some indication of potential for asymmetric cardiac hypertrophy [72] or regional dysfunction in dilated cardiomyopathy [73]. The diagnosis of efficiency heterogeneity could allow for mechanical therapy in the form of a novel implantable hydrogel treatment [74] to be applied more locally to relieve areas of wall stress where it is needed most. Also, therapy in the form of resynchronization [56], [75], [76] does not necessarily provide a uniform response of cardiac efficiency [76] or the onset of LV contraction and this may also be true of Left Ventricular Assist Devices (LVAD) [77]. The assessment of efficiency heterogeneity would be able to evaluate the prognosis of these types of therapies for HF patients.

The physiology of the heart is complex involving the conversion of chemical energy into mechanical energy. The question of how much energy is expended in a piece of myocardial tissue is thought-provoking and difficult to answer. Seeking an answer opens up a milieu of physics, chemistry, and mathematical questions. For example, even describing the transformation of a piece of tissue from an undeformed to a deformed state requires complex tensor calculus. However, the formulation of the physics, chemistry, and mathematical principles are key to developing a comprehensive model of the energy expenditure in a piece of myocardial tissue and answers that such a model can provide is vital to the understanding of the true health of the heart. PET/MRI imaging of the heart provides simultaneous measures of biochemistry and biomechanics that can be used to interrogate the energy expenditure through measures of myocardial tissue efficiency to better understand disease processes in diagnosis and threptic intervention of cardiac disease.

Acknowledgment

We acknowledge support from Dassault Systemes SIMULIA Corporation, Johnston, RI, in providing access to the Living Heart Model in the Abaqus software package for our work.

This work was supported in part by the National Institutes of Health under Grant Nos. R01 EB026332, and R01 HL135490.

Appendix

The following provides the details in the derivation of the strain tensor in the deformed Lagrandian curvilinear coordinates. We remind the readers that the Lagrangian curvilinear coordinates are shown in Fig. 2. The goal here is to present the equations in the derivation between (8) and (10) that is not presented in [31].

First, let’s begin with the expression for the strain in terms of the difference between deformed and undeformed surfaces:

$$ds^2 - ds_0^2 = d\boldsymbol{R}\cdot d\boldsymbol{R} - d\boldsymbol{r}\cdot d\boldsymbol{r} = 2\gamma_{ij}d\xi^i d\xi^j, \tag{3}$$

Again, we write the differential of the position vector $\boldsymbol{r}$ in the undeformed curvilinear coordinates:

$$d\boldsymbol{r} = \frac{\partial \boldsymbol{r}}{\partial \xi_i}d\xi_i = \boldsymbol{g}_i d\xi_i, \tag{4}$$

and the differential of the position vector $\boldsymbol{R}$ in the undeformed curvilinear coordinates:

$$\begin{aligned} d\boldsymbol{R} &= \frac{\partial \boldsymbol{R}}{\partial \xi_i}d\xi_i = \frac{\partial}{\partial \xi_i}(\boldsymbol{r}+\boldsymbol{u})d\xi_i, \\ &= \left(\boldsymbol{g}_i + \frac{\partial \boldsymbol{u}}{\partial \xi_i}\right)d\xi_i\,. \end{aligned} \tag{5}$$

Using (2), the partial derivative of the displacement vector $\boldsymbol{u}$ expressed in terms of the contravariant tangent vectors $\boldsymbol{g}^j$ is

$$\begin{aligned} \frac{\partial \boldsymbol{u}}{\partial \xi_i} &= \frac{\partial}{\partial \xi_i}\left(u_j \boldsymbol{g}^j\right) = \frac{\partial u_j}{\partial \xi_i}\boldsymbol{g}^j + u_j\frac{\partial \boldsymbol{g}^j}{\partial \xi_i}, \\ &= \frac{\partial u_j}{\partial \xi_i}\boldsymbol{g}^j - u_j \Gamma_{ik}^j \boldsymbol{g}^k\,. \end{aligned} \tag{6}$$

Therefore

$$d\boldsymbol{R} = \left(\boldsymbol{g}_i + \frac{\partial u_j}{\partial \xi_i}\boldsymbol{g}^j - u_j\Gamma_{ik}^j\boldsymbol{g}^k\right)d\xi_i = \left(\boldsymbol{g}_i + \boldsymbol{u}_{,i}\right)d\xi_i, \tag{7}$$

where $\boldsymbol{u}_{,i}$ denotes the partial derivative $\frac{\partial \boldsymbol{u}}{\partial \xi_i}$, and $\boldsymbol{g}_i$ and $\boldsymbol{g}^j$ are covariant and contravariant vectors in the undeformed state, respectively. Substituting the expressions for $d\boldsymbol{R}$ in (7) and for $d\boldsymbol{r}$ in (4) into the following expression for strain:

$$ds^2 - ds_0^2 = d\boldsymbol{R}\cdot d\boldsymbol{R} - d\boldsymbol{r}\cdot d\boldsymbol{r},$$

we have

$$\begin{aligned} ds^2 - ds_0^2 &= \left(\boldsymbol{g}_i + \frac{\partial u_m}{\partial \xi_i}\boldsymbol{g}^m - u_m\frac{\partial^2 z_n}{\partial \xi_k \partial \xi_i}\frac{\partial \xi_m}{\partial z_n}\boldsymbol{g}^k\right)d\xi_i \\ &\cdot \left(\boldsymbol{g}_j + \frac{\partial u_{m'}}{\partial \xi_j}\boldsymbol{g}^{m'} - u_{m'}\frac{\partial^2 z_{n'}}{\partial \xi_{k'}\partial \xi_j}\frac{\partial \xi_{m'}}{\partial z_{n'}}\boldsymbol{g}^{k'}\right)d\xi_j - \boldsymbol{g}_i d\xi_i \cdot \boldsymbol{g}_j d\xi_j \\ &= \left(\boldsymbol{g}_i + \frac{\partial u_m}{\partial \xi_i}\boldsymbol{g}^m - u_m\Gamma_{ik}^m\boldsymbol{g}^k\right)d\xi_i \cdot \left(\boldsymbol{g}_j + \frac{\partial u_{m'}}{\partial \xi_i}\boldsymbol{g}^{m'} - u_{m'}\Gamma_{jk'}^{m'}\boldsymbol{g}^{k'}\right)d\xi_j - \boldsymbol{g}_i d\xi_i \cdot \boldsymbol{g}_j d\xi_j, \\ &= \left(\boldsymbol{g}_i + \boldsymbol{u}_{,i}\right)\cdot\left(\boldsymbol{g}_j + \boldsymbol{u}_{,j}\right)d\xi_i d\xi_j - \boldsymbol{g}_i\cdot\boldsymbol{g}_j d\xi_i d\xi_j, \\ &= \left(\boldsymbol{g}_i\cdot\boldsymbol{g}_j + \boldsymbol{u}_{,i}\cdot\boldsymbol{g}_j + \boldsymbol{g}_i\cdot\boldsymbol{u}_{,j} + \boldsymbol{u}_{,i}\cdot\boldsymbol{u}_{,j}\right)d\xi_i d\xi_j - \boldsymbol{g}_i\cdot\boldsymbol{g}_j d\xi_i d\xi_j, \end{aligned} \tag{A1}$$

where the partial derivative $\boldsymbol{u}_{,i} = \frac{\partial \boldsymbol{u}}{\partial \xi_i}$ is expressed in terms of the contravariant tangent vectors $\boldsymbol{g}^j$:

$$\boldsymbol{u}_{,i} = \left(u_j \boldsymbol{g}^j\right)_{,i} = \left(u_{j,i}\boldsymbol{g}^j - \Gamma^j_{ik} u_j \boldsymbol{g}^k\right),$$

or is expressed in terms of covariant tangent vectors $\boldsymbol{g}_j$:

$$\boldsymbol{u}_{,i} = \left(u^j \boldsymbol{g}_j\right)_{,i} = \left(u^j_{,i}\boldsymbol{g}_j + \Gamma^k_{ji} u^j \boldsymbol{g}_k\right).$$

Substituting the following expressions into (A1)

$$\begin{aligned}\boldsymbol{u}_{,i}\cdot\boldsymbol{g}_j &= \left(u_{m,i}\boldsymbol{g}^m - \Gamma^m_{ik}u_m\boldsymbol{g}^k\right)\cdot\boldsymbol{g}_j \\ &= \left(u_{m,i}\delta_{mj} - \Gamma^m_{ik}u_m\delta_{kj}\right) = u_{j,i} - \Gamma^m_{ij}u_m,\end{aligned}$$

$$\begin{aligned}g_i\cdot\boldsymbol{u}_{,j} &= \boldsymbol{g}_i\cdot\left(u_{m,j}\boldsymbol{g}^m - \Gamma^m_{jk}u_m\boldsymbol{g}^k\right) \\ &= \left(u_{m,j}\delta_{im} - \Gamma^m_{jk}u_m\delta_{ik}\right) = u_{i,j} - \Gamma^m_{ji}u_m,\end{aligned}$$

we have

$$\begin{aligned}ds^2 - ds_0^2 &= \left(u_{j,i} - \Gamma^m_{ij}u_m + u_{i,j} - \Gamma^m_{ji}u_m\boldsymbol{u}_{,i}\cdot\boldsymbol{u}_{,j}\right)d\xi_i d\xi_j, \\ &= \left(u_{i,j} - \Gamma^m_{ij}u_m + u_{j,i} - \Gamma^m_{ji}u_m + \boldsymbol{u}_{,i}\cdot\boldsymbol{u}_{,j}\right)d\xi_i d\xi_j, \\ &= \left(u_{i|j} + u_{j|i} + \boldsymbol{u}_{,i}\cdot\boldsymbol{u}_{,j}\right)d\xi_i d\xi_j,\end{aligned} \tag{A2}$$

where $u_{i|j} = u_{i,j} - \Gamma^m_{ij}u_m$ is the covariant derivative of the displacement vector $\boldsymbol{u}$.

Remember $\boldsymbol{u}_{,i}$ can be expressed in term of covariant tangent vectors $\boldsymbol{g}_j$ or contravariant tangent vectors $\boldsymbol{g}^j$. Here we choose to express

$$\boldsymbol{u}_{,i}\cdot\boldsymbol{u}_{,j} = \left(u^{m'}_{,i}\boldsymbol{g}_{m'} + \Gamma^{k'}_{m'i}u^{m'}\boldsymbol{g}_{k'}\right)\cdot\left(u_{m,j}\boldsymbol{g}^m - \Gamma^m_{jk}u_m\boldsymbol{g}^k\right)$$

in (A2); thus, yielding

$$\begin{aligned}\boldsymbol{u}_{,i}\cdot\boldsymbol{u}_{,j} &= u^k_{,i}u_{m,j}\boldsymbol{g}_k\cdot\boldsymbol{g}^m + \Gamma^k_{m'i}u^{m'}u_{m,j}\boldsymbol{g}_k\cdot\boldsymbol{g}^m - u^k_{,i}\Gamma^{m'}_{jm}u_{m'}\boldsymbol{g}_k\cdot\boldsymbol{g}^m - \Gamma^k_{m'i}u^{m'}\Gamma^n_{jm}u_n\boldsymbol{g}_k\cdot\boldsymbol{g}^m, \\ &= u^k_{,i}u_{m,j}\delta_{km} + \Gamma^k_{m'i}u^{m'}u_{m,j}\delta_{km} - u^k_{,i}\Gamma^{m'}_{jm}u_{m'}\delta_{km} - \Gamma^k_{m'i}u^{m'}\Gamma^n_{jk}u_n\delta_{km}, \\ &= u^m_{,i}u_{m,j} + \Gamma^m_{m'i}u^{m'}u_{m,j} - u^m_{,i}\Gamma^{m'}_{jm}u_{m'} - \Gamma^m_{m'i}u^{m'}\Gamma^n_{jm}u_n.\end{aligned}$$

Substituting k for m', we have

$$\boldsymbol{u}_{,i}\cdot\boldsymbol{u}_{,j} = u^m_{,i}u_{m,j} + \Gamma^m_{ki}u^k u_{m,j} - u^m_{,i}\Gamma^k_{mj}u_k - \Gamma^m_{ik}u^k\Gamma^n_{mj}u_n. \tag{A3}$$

The strain tensor is always covariant where coordinate lines ξ_i are expected to convect to contravariant form ξ^i. Therefore, the measure of strain in terms of contravariant coordinates ξ^i and strain tensor γ_{ij} is

$$ds^2 - ds_0^2 = \left(u_{i|j} + u_{j|i} + \boldsymbol{u}_{,i} \cdot \boldsymbol{u}_{,j}\right) d\xi^i d\xi^j . \tag{A4}$$

Substituting (A3) into (A4), we have

$$\begin{aligned} ds^2 - ds_0^2 &= \left(u_{i|j} + u_{j|i} + u^m_{,i} u_{m,j} + \Gamma^m_{ki} u^k u_{m,j} - u^m_{,i} \Gamma^k_{mj} u_k - \Gamma^m_{ik} u^k \Gamma^n_{mj} u_n\right) d\xi^i d\xi^j, \\ &= \left(u_{i|j} + u_{j|i} + \left[u^m_{,i} + \Gamma^m_{ik} u^k\right]\left[u_{m,j} - \Gamma^n_{mj} u_n\right]\right) d\xi^i d\xi^j \\ &= \left(u_{i|j} + u_{j|i} + u^m_{|i} u_{m|j}\right) d\xi^i d\xi^j = 2\gamma_{ij} d\xi^i d\xi^j . \end{aligned} \tag{A5}$$

where $u^m_{|i} = u^m_{,i} + \Gamma^m_{ik} u^k$.

References

[1]. Virani SS, et al., “Heart Disease and Stroke Statistics-2020 Update: A Report from the American Heart Association,” Circulation, vol. 141, no. 9, pp. e139–e596, 2020. [PubMed: 31992061]

[2]. Fields LE, Burt VL, Cutler LA, Hughes J, Roccella EJ, Sorlie P, “The burden of adult hypertension in the United States 1999 to 2000: A rising tide. Hypertension,” vol. 44, pp. 398–404, 2004. [PubMed: 15326093]

[3]. Hernandez AM, et al., “Longitudinal evaluation of left ventricular substrate metabolism, perfusion, and dysfunction in the SHR model of hypertrophy using microPET imaging,” J Nucl Med, vol.54, pp.1938–45, 2013. [PubMed: 24092939]

[4]. Huber JS, et al., “Longitudinal evaluation of myocardial fatty acid and glucose metabolism in fasted and nonfasted spontaneously hypertensive rats using microPET/CT,” Molecular Imaging, 2017.

[5]. Lopaschuk GD, Ussher JR, Folmes CDL, Jaswal JS, Stanley WC, “Myocardial fatty acid metabolism in health and disease,” Physiol Rev, vol. 90, pp. 207–258, 2010. [PubMed: 20086077]

[6]. Macron L, et al., “Global circumferential left ventricular strain impairment in hypertrophic cardiomyopathy: Comparison to left ventricular hypertrophy and late gadolinium enhancement,” J Cardiovas Magn Reson, vol. 15(Suppl 1), pp. E122, 2013.

[7]. de las Fuentes L, et al., “Hypertensive left ventricular hypertrophy is associated with abnormal myocardial fatty acid metabolism and myocardial efficiency,” J Nucl Cardiol, vol. 13, pp. 369–77, 2006. [PubMed: 16750782]

[8]. Bing RJ, et al. “The measurement of coronary blood flow, oxygen consumption, and efficiency of the left ventricle in man,” Am Heart J, vol. 138, pp. 1–24, 1949.

[9]. Armbrecht JJ, Buxton DB, Brunken RC, Phelps ME, Schelbert HR, “Regional myocardial oxygen consumption determined noninvasively in humans with [1–11C]acetate and dynamic positron tomography,” Circulation, vol. 80, pp. 863–872, 1989. [PubMed: 2791250]

[10]. Porenta G, Cherry S, Czernin J, Brunken R, Kuhle W, Hashimoto T, Schelbert HR, “Noninvasive determination of myocardial blood flow, oxygen consumption and efficiency in normal humans by carbon-11 acetate positron emission tomography imaging,” Eur J Nucl Med, vol. 26, pp. 1465–74, 1999. [PubMed: 10552089]

[11]. Harms HJ, et al. “Automatic calculation of myocardial external efficiency using a single ^{11}C-acetate PET scan,” J Nucl Cardiol, vol. 25, pp. 1937–44, 2018. [PubMed: 29946824]

[12]. van den Hoff J, Burchert W, Wolpers HG, Meyer GJ, Hunde-shagen H, “A kinetic model for cardiac PET with [1-carbon-11]-acetate,” J Nucl Med, vol. 37, pp. 521–29, 1996. [PubMed: 8772659]

[13]. Sun KT, et al. Simultaneous measurement of myocardial oxygen consumption and blood flow using [1-carbon-11]acetate," J Nucl Med, vol. 39, pp. 272–80, 1998. [PubMed: 9476935]

[14]. Chan SY, Brunken RC, Phelps ME, Schelbert HR, "Use of the metabolic tracer carbon-11-acetate for evaluation of regional myocardial perfusion," J Nucl Med, vol. 32, pp. 665–72, 1991. [PubMed: 2013805]

[15]. van den Hoff J, et al. "[1-11C]Acetate as a quantitative perfusion tracer in myocardial PET," J Nucl Med, vol. 42, pp. 1174–82, 2001. [PubMed: 11483676]

[16]. Bastos MB, et al., "Invasive left ventricle pressure-volume analysis: Overview and practical clinical implications," Eur Heart J, vol. 41, no. 12, pp. 1286–97, 2020. [PubMed: 31435675]

[17]. Guccione JM, McCulloch AD, "Mechanics of active contraction in cardiac muscle: Part I—Constitutive relations for fiber stress that describe deactivation" J Biomech Eng, vol. 115, pp. 72–81, 1993. [PubMed: 8445901]

[18]. Guccione JM, Waldman LK, McCulloch AD, "Mechanics of active contraction in cardiac muscle: Part II—Cylindrical models of the systolic left ventricle," J Biomech Eng, vol. 115, pp. 82–90, 1993. [PubMed: 8445902]

[19]. Veress AI, Segars WP, Weiss JA, Tsui BM, Gullberg GT, "Normal and pathological NCAT image and phantom data based on physiologically realistic left ventricle finite-element models," IEEE Trans Med Imag, vol. 25, pp. 1604–16, 2006.

[20]. Veress AI, Segars WP, Tsui BM, Gullberg GT, "Incorporation of a left ventricle finite element model defining infarction into the XCAT imaging phantom," IEEE Trans Med Imag, vol. 30, pp. 915–27, 2011.

[21]. Veress AI, et al. "Regional changes in the diastolic deformation of the left ventricle for SHR and WKY rats using ^{18}FDG based microPET technology and hyperelastic warping," ANN Biomed Eng, vol. 36, pp. 1104–17, 2008. [PubMed: 18437574]

[22]. Wenk JF, et al., "First evidence of depressed contractility in the border zone of a human myocardial infarction," The Ann Thorac Surg, vol. 93, pp. 1188–93, 2012. [PubMed: 22326127]

[23]. Cupps BP, et al., "Severe aortic insufficiency and normal systolic function: Determining regional left ventricular wall stress by finite-element analysis, Ann Thorac Surg, vol. 76, pp. 668–75, 2003. [PubMed: 12963173]

[24]. Baillargeon B, Rebelo N, Fox DD, Taylor RL, Kuhl E, "The Living Heart Project: A robust and integrative simulator for human heart function," Eur J Mech A-Solid, vol. 48, pp. 38–47, 2014.

[25]. SIMULIA Living Heart Human Model User Guide. LHHM 2.1 Beta Release, 3, 2018.

[26]. Abaqus 6.13. Analysis User's Manual, 2014. Simulia. Dassault Systèmes.

[27]. Maas SA, Ellis BJ, Ateshian GA, Weiss JA, "FEBio: Finite elements for biomechanics," J Biomech Eng, vol. 134, no. 1, pp. 011005, 2012. [PubMed: 22482660]

[28]. I Veress A, Gullberg GT, Weiss JA, "Measurement of strain in the left ventricle during diastole with cine-MRI and deformable image registration, "J Biomechan Eng, vol. 127, pp. 1195–1207, 2005.

[29]. Carruth ED, McCulloch AD, Omens JH, "Transmural gradients of myocardial structure and mechanics: Implications for fiber stress and strain in pressure overload," Prog Biophys Mol Biol, vol. 122, pp. 21526, 2016.

[30]. Gibbs CL, "Cardiac energetics," Physiol Rev, vol. 58, pp. 174–254, 1978. [PubMed: 146205]

[31]. Chung TG, Applied Continuum Mechanics. Cambridge, UK: Cambridge University Press, 1996.

[32]. Hunter PJ, Nash MP, Sands GB, "Computational electromechanics of the heart," In: Computational Biology of the Heart. (Panfilov AV, Holden AV, eds.) Chichester, UK: John Wiley & Sons, 1997.

[33]. Bonet J, Wood RD, Nonlinear Continuum Mechanics for Finite Element Analysis. Cambridge, UK: Cambridge University Press, 1997.

[34]. Humphrey JD, Cardiovascular Solid Mechanics: Cells, Tissues, and Organs. New York, NY: Springer-Verlag, 2002.

[35]. Dorri F, Niederer PF, Lunkenheimer PP, "A finite element model of the human left ventricular systole," Comput Methods Biomechs Biomed Engin, vol. 9, no. 5, pp. 319–341, 2006.

[36]. Moore CC, Lugo-Olivieri CH, McVeigh ER, Zerhouni EA, "Three-dimensional systolic strain patterns in the normal human left ventricle: characterization with tagged MR imaging," Radiology, vo. 214, pp. 453–466, 2000. [PubMed: 10671594]

[37]. Gsell MAF, Augustin CM, Prassl AJ, Karabelas E, Fernandes JF, Kelm M, Goubergrits L, Kuehne T, Plank G, "Assessment of wall stresses and mechanical heart power in the left ventricle: Finite element modeling versus Laplace analysis," Int J Numer Method Biomed Eng, vol. 34, no. 12, e3147, 2018. [PubMed: 30151998]

[38]. Lee LC, et al., "Analysis of patient-specific surgical ventricular restoration: importance of an ellipsoidal left ventricular geometry for diastolic and systolic function," J Appl Physiol, vol. 115, pp. 136–44, 2013. [PubMed: 23640586]

[39]. Gaasch WH, Battle WE, Oboler AA, Banas JS Jr., Levine HJ, "Left ventricular stress and compliance in man with special reference to normalized ventricular function curves," Circulation, vol. XLV, pp. 747–62, 1972.

[40]. Holzapfel GA, Ogden RW, "Constitutive modelling of passive myocardium: A structurally based framework for material characterization," Phil Trans A, vol. 367, pp. 3445–75, 2009.

[41]. Conduction System Tutorial: Gap Junctions (Cell-to-Cell Conduction), http://www.vhlab.umn.edu/atlas/conduction-system-tutorial/gap-junctions.shtml.

[42]. Nagumo J, Arimoto S, Yoshizawa S, "An active pulse transmission line simulating nerve axon," Proc Inst Radio Eng, vol. 50, pp. 2061–70, 1962.

[43]. Rischpler C, et al., "Cardiac PET/MRI: Current clinical status and future perspectives," Semin Nucl Med, vol. 50, no. 3, pp. 260–69, 2020. [PubMed: 32284112]

[44]. Kunze KP, et al. "Quantitative cardiovascular magnetic resonance: Extracellular volume, native T1 and ^{18}F-FDG PET/CMR imaging in patients after revascularized myocardial infarction and association with markers of myocardial damage and systemic inflammation," J Cardiovasc Magn Reson, vol. 20, no. 33, 2018.

[45]. Takeishi Y, Masuda A, Kubo H, Tominaga H, Oriuchi N, Takenoshita S, "Cardiac imaging with 18F-fluorodeoxyglucose PET/MRI in hypertrophic cardiomyopathy," J Nucl Cardiol, vol. 24, no. 5, pp. 1827–28, 2017. [PubMed: 27743298]

[46]. Lau JM, Laforest R, Nensa F, Zheng J, Gropler RJ, Woodard PK, "Cardiac applications of PET/MR imaging," Magn Reson Imag Clin N Am, vol. 25, no. 2, pp. 325–33, 2017.

[47]. Kunze KP, et al., "Myocardial perfusion quantification using simultaneously acquired ^{13}NH3-ammonia PET and dynamic contrast-enhanced MRI in patients at rest and stress," Magn Reson Med, vol. 80, pp. 264154, 2018.

[48]. Beadle RM, et al., "Metabolic manipulation in chronic heart failure study protocol for randomized controlled trial," Trials, vol. 12, pp. 140, 2011. [PubMed: 21645332]

[49]. Amado LC, et al., "Multimodality noninvasive imaging demonstrates in vivo cardiac regeneration after mesenchymal stem cell therapy," J Am Coll Cardiol, vol. 48, pp. 2116–24. 2006. [PubMed: 17113001]

[50]. Bengel FM, "PET-based myocardial efficiency: Powerful yet underutilized-now simpler than ever," J Nucl Cardiol, vol. 25, pp. 1945–47, 2018. [PubMed: 30097851]

[51]. Knaapen P, Germans T, Knuuti J, Paulus WJ, Dijkmans PA, Allaart CP, Lammertsma AA, Visser FC, "Myocardial energetics and efficiency: Current status of the noninvasive approach," Circulation, vol. 115, pp. 918–27, 2007. [PubMed: 17309938]

[52]. Beanlands RS, Nahmias C, Gordon E, Coates G, deKemp R, Firnau G, Fallen E, "The effects of beta(1)-blockade on oxidative metabolism and the metabolic cost of ventricular work in patients with left ventricular dysfunction: A double-blind, placebo-controlled, positron-emission tomography study," Circulation, vol. 102, pp. 2070–5, 2000. [PubMed: 11044422]

[53]. Ukkonen H, et al., "Effect of cardiac resynchronization on myocardial efficiency and regional oxidative metabolism," Circulation, vol. 107, pp. 28–31, 2003. [PubMed: 12515738]

[54]. Hall AB, et al., "Effects of short-term continuous positive airway pressure on myocardial sympathetic nerve function and energetics in patients with heart failure and obstructive sleep apnea: A randomized study," Circulation, vol. 130, pp. 892–901, 2014. [PubMed: 24993098]

[55]. Stolen KQ, et al., “Exercise training improves biventricular oxidative metabolism and left ventricular efficiency in patients with dilated cardiomyopathy,” J Am Coll Cardiol, vol. 41, pp. 460–7, 2003. [PubMed: 12575976]

[56]. Lindner O, Sorensen J, Vogt J, Fricke E, Baller D, Horstkotte D, Burchert W, “Cardiac efficiency and oxygen consumption measured with 11C-acetate PET after long-term cardiac resynchronization therapy,” J Nucl Med, vol. 47, pp. 378–83, 2006. [PubMed: 16513605]

[57]. How OJ, Aasum E, Severson DL, Chan WY, Essop MF, S Larsen T, “Increased myocardial oxygen consumption reduces cardiac efficiency in diabetic mice,” Diabetes, vol. 55, pp. 466–73, 2006. [PubMed: 16443782]

[58]. Clemmensen TS, et al., “Myocardial oxygen consumption and efficiency in patients with cardiac amyloidosis,” J Am Heart Assoc, vol. 7, no. 21, pp. e009974, 2018. [PubMed: 30571379]

[59]. Bengel FM, Ueberfuhr P, Schiepel N, Nekolla SG, Reichart B, Schwaiger M, “Myocardial efficiency and sympathetic reinnervation after orthotopic heart transplantation: A noninvasive study with positron emission tomography,” Circulation, vol. 103, pp. 1881–6, 2001. [PubMed: 11294807]

[60]. Yaniv Y, Juhaszova M, Sollott SJ, “Age-related changes of myocardial ATP supply and demand mechanisms,” Trends Endocrinol Metab, vol. 24, pp. 495–505, 2013. [PubMed: 23845538]

[61]. Barton GP, Vildberg L, Goss K, Aggarwal N, Eldridge M, McMillan AB, “Simultaneous determination of dynamic cardiac metabolism and function using PET/MRI,” J Nucl Cardiol, vol. 26, pp. 1946–57, 2019. [PubMed: 29717407]

[62]. Paterson DI, O’Meara E, Chow BJ, Ukkonen H, Beanlands RS, “Recent advances in cardiac imaging for patients with heart failure,” Curr Opin Cardiol, vol. 26, pp. 132–43, 2011. [PubMed: 21297464]

[63]. Wollmuth JR, et al., “Left ventricular wall stress in patients with severe aortic insufficiency with finite element analysis,” Ann Thorac Surg, vol. 82, pp. 840–6, 2006. [PubMed: 16928495]

[64]. Veress AI, Klein G, Gullberg GT, “A comparison of hyperelastic warping of PET images with tagged MRI for the analysis of cardiac deformation,” Intern J Biomed Imag, 728624, doi:10.1155/2013/728624, 2013.

[65]. Giannakidis A, Rohmer D, AI Veress GT Gullberg, Chapter 53: “Diffusion tensor MRI-derived myocardial fiber disarray in hypertensive left ventricular hypertrophy: Visualization, quantification and the effect on mechanical function,” Cardiac Mapping, Eds: Shenasa M, Hindricks G, Borggrefe M, Breithardt G, Josephson ME (Blackwell Publishing Limited, Chichester, West Sussex, United Kingdom), 2013.

[66]. Khalique Z, et al., “Diffusion tensor cardiovascular magnetic resonance in cardiac amyloidosis,” JACC Cardiovasc Imaging, vol. 13, pp. 1235–55, 2020. [PubMed: 31607663]

[67]. Mekkaoui C, Reese TG, Jackowski MP, Bhat H, Sosnovik DE, “Diffusion MRI in the heart,” NMR Biomed, vol. 30, no. 3, pp. e3426, 2017.

[68]. Buck A, Wolpers HG, Hutchins GD, Savas V, Mangner TJ, Nguyen N, Schwaiger M, “Effect of carbon-11-acetate recirculation on estimates of myocardial oxygen consumption by PET,” J Nucl Med, vol. 32, pp. 1950–7, 1991. [PubMed: 1919738]

[69]. Soto PF, et al., “Impact of aging on myocardial metabolic response to dobutamine,” Am J Physiol Heart Circ Physiol, vol. 285, pp. H2158–64, 2003. [PubMed: 12881222]

[70]. Gropler RJ, “Noninvasive measurements of myocardial oxygen consumption - can we do better?” J Am Coll Cardiol, vol. 41, pp. 468–70, 2003. [PubMed: 12575977]

[71]. Hutchins GD, et al., “PET imaging of oxidative metabolism abnormalities in sympathetically denervated canine myocardium,” J Nucl Med, vol. 40, pp. 846–53, 1999. [PubMed: 10319760]

[72]. Güçlü A, et al., “ENerGetIcs in hypertrophic cardiomyopathy: Translation between MRI, PET and cardiac myofilament function (ENGINE study),” Neth Heart J, vol. 21, pp. 567–71, 2013. [PubMed: 24114686]

[73]. Tegtmeyer LC, et al., “Multiple phenotypes in phosphoglucomutase 1 deficiency,” N Engl J M, vol. 370, pp. 533–42, 2014. [PubMed: 24499211]

[74]. Lee LC, et al., “Algisyl-LVR with coronary artery bypass grafting reduces left ventricular wall stress and improves function in the failing human heart,” Int J Cardiol, vol. 168, pp. 2022–8, 2013. [PubMed: 23394895]

[75]. Braunwald E, “The ten advances that have defined modern cardiology,” Trends Cardiovasc Med, vol. 24, pp. 179–83, 2014. [PubMed: 25017918]

[76]. Ukkonen H, et al., “Effect of cardiac resynchronization on myocardial efficiency and regional oxidative metabolism,” Circulation, vol. 107, pp. 28–31, 2003. [PubMed: 12515738]

[77]. Rose EA, et al. [Randomized Evaluation of Mechanical Assistance for the Treatment of Congestive Heart Failure (REMATCH) Study Group], “Long-term use of a left ventricular assist device for end-stage heart failure,” N Engl J M, vol. 345, no. 20, pp. 1435–43, 2018.

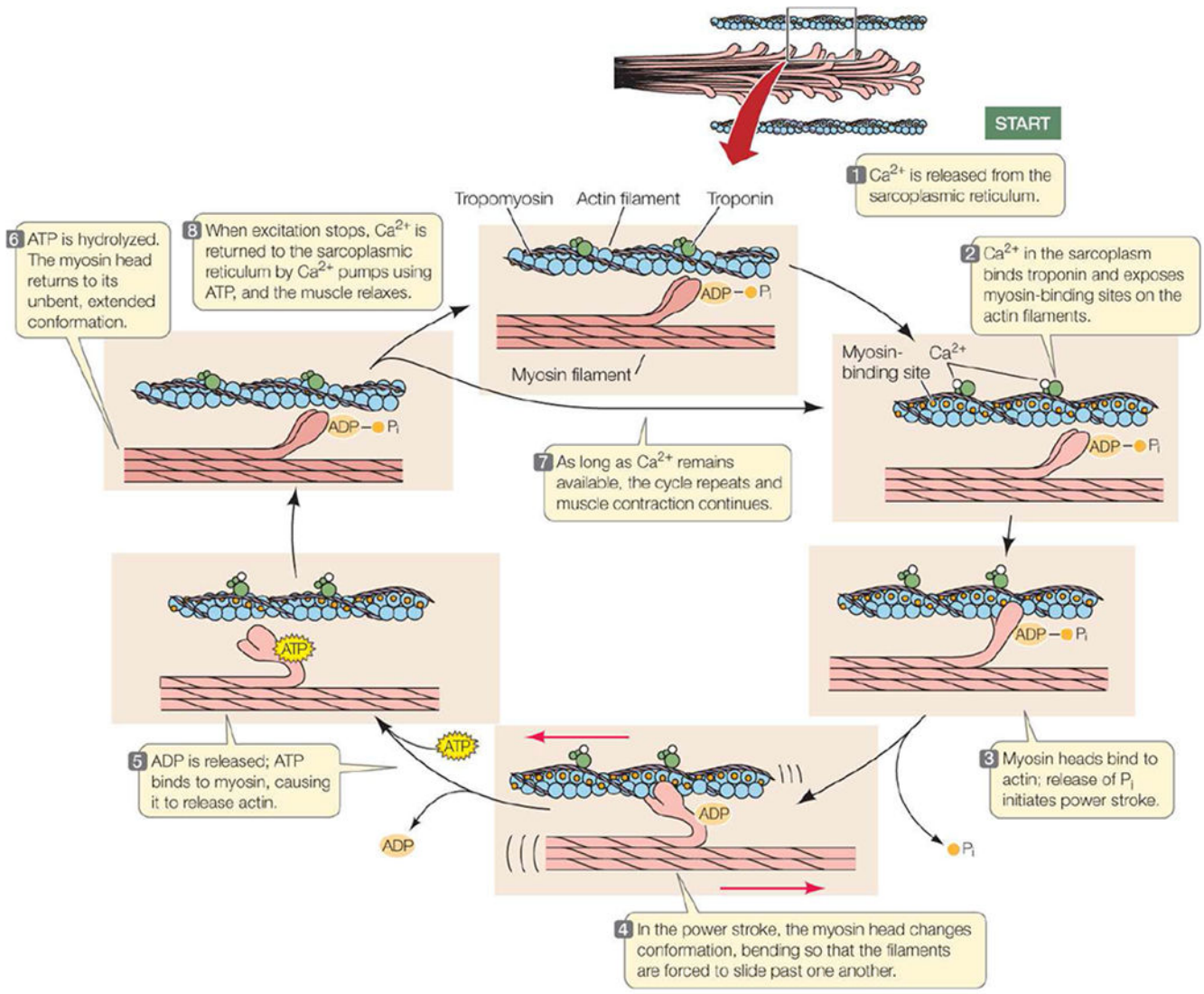

Fig. 1.

Sliding filament model of muscle contraction. Calcium released from sarcoplasmic reticulum initially binds to troponin-C resulting in conformational change of tropomyosin and exposes myosin-binding sites on the actin filament so that myosin heads can bind to actin. A power stroke results where ADP and inorganic phosphate are released from the myosin head so that myosin head can pivot and bend, pulling on the actin causing muscle contraction. A new molecule of ATP binds to the myosin head, causing it to detach from the actin. Finally, ATP is hydrolyzed into ADP and inorganic phosphate, causing the myosin heads to relax so that the cycle of contraction can begin again. With relaxation intracellular calcium is reduced: 1) by entering the sarcoplasmic reticulum for storage via a sarcoendoplasmic reticulum calcium-ATPase channel at the expense of an ATP molecule; and 2) through a sodium-calcium exchange channel which extrudes a calcium ion and admits a sodium ion when membrane repolarization starts. Calcium is no longer bound to troponin C. (Reprinted from www.macmillanhighered.com).

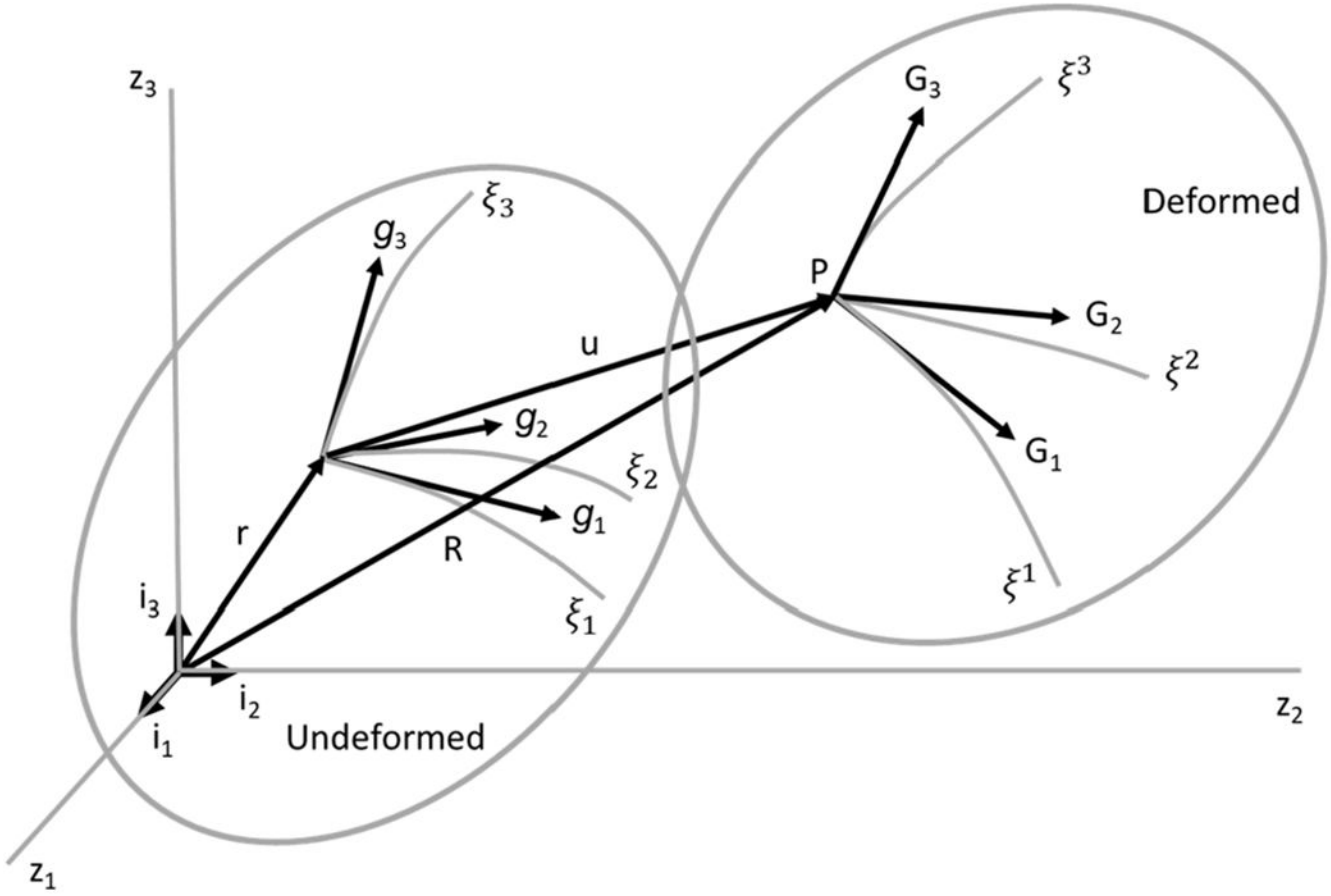

Fig. 2.

Lagrangian curvilinear coordinates. The Lagrangian curvilinear covariant coordinates (ξ_1, ξ_2, ξ_3) for the undeformed state are convected into the Lagrangian curvilinear contravariant coordinates (ξ^1, ξ^2, ξ^3) in the deformed state. The tangent vectors ($\boldsymbol{g}^1$, $\boldsymbol{g}^2$, $\boldsymbol{g}^3$) are tangent to the undeformed curvilinear covariant coordinates (ξ_1, ξ_2, ξ_3), whereas the tangent vectors ($\boldsymbol{G}_1$, $\boldsymbol{G}_2$, $\boldsymbol{G}_3$) are tangent to the deformed curvilinear contravariant coordinates (ξ^1, ξ^2, ξ^3). (Drawn based on Figure 2.3.1 in [31] but modified to indicate that here we assume that the undeformed covariant coordinates (ξ1, ξ2 ,ξ3) are convected into deformed contravariant coordinates (ξ^1, ξ^2, ξ^3).

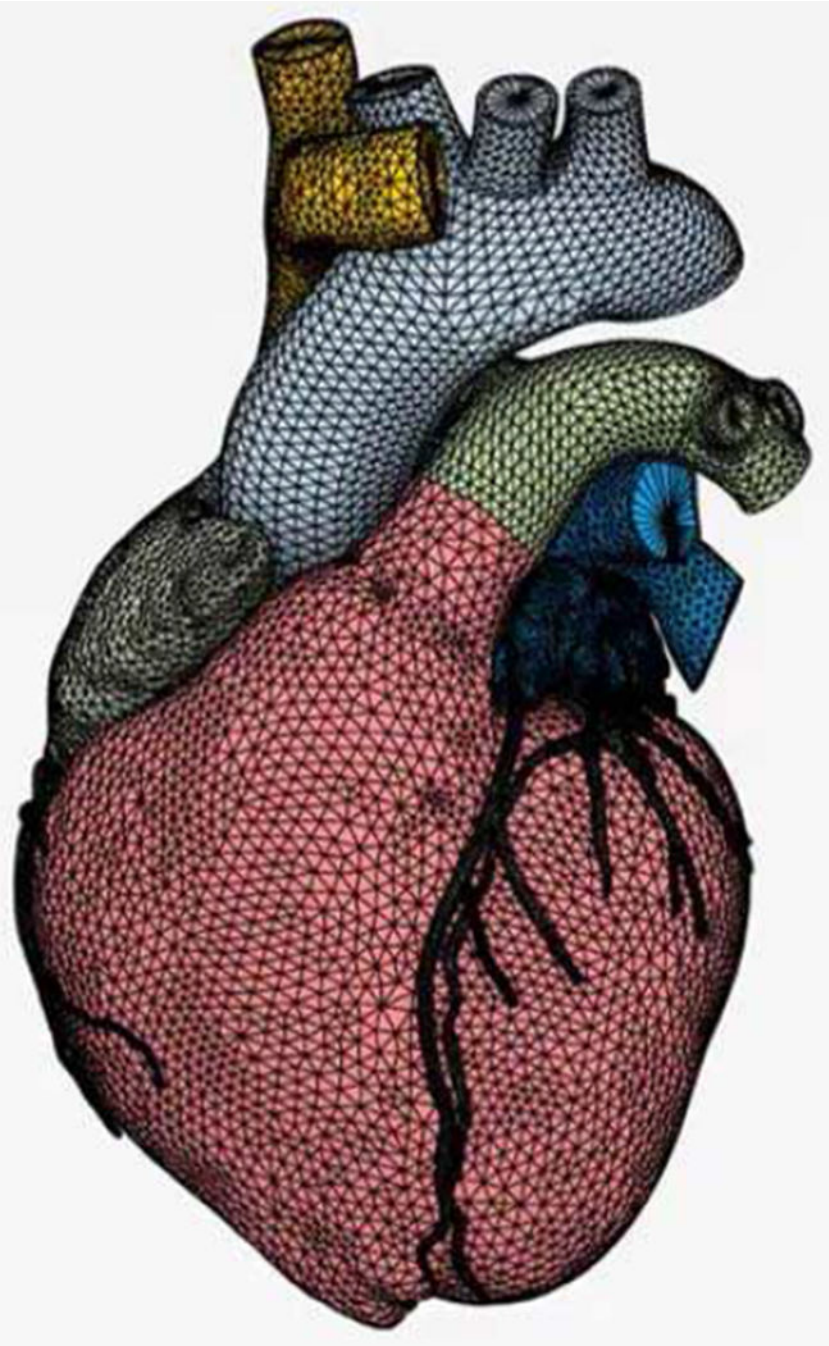

Fig. 3.

Living Heart Model (LHM). The LHM as described in [24], [25] includes the aortic arch, valves, coronary arteries and veins, pulmonary trunk, left and right atria and ventricles, papillary muscles and chordae tendineae, superior and inferior vena cava, mechanical tissue properties, and electrical stimulation. (Image from Dassault Systèmes).

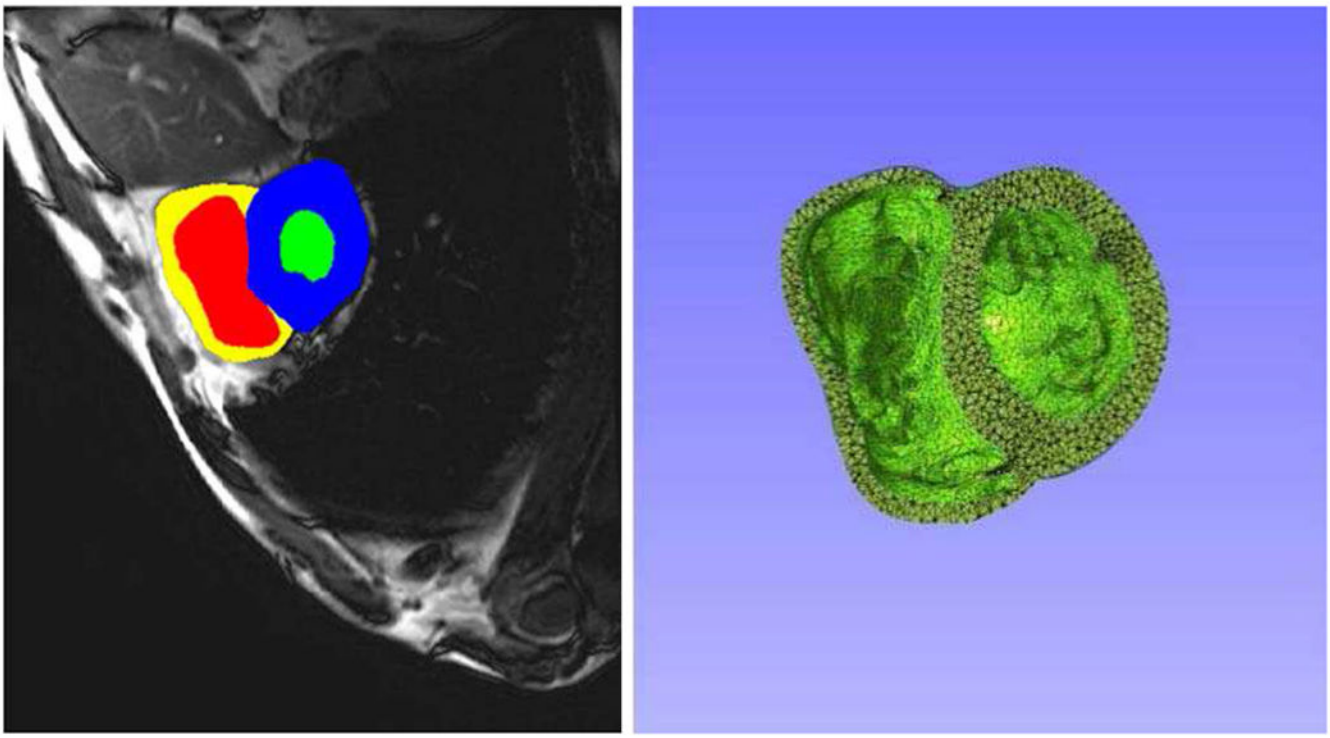

Fig. 4.

Left: Segmented left (blue and green) and right ventricle (yellow and red) from the patient cardiac cine MRI data. Right: LHM after warping to the patient segmented MRI slice. This is reanalyzed in Abaqus.

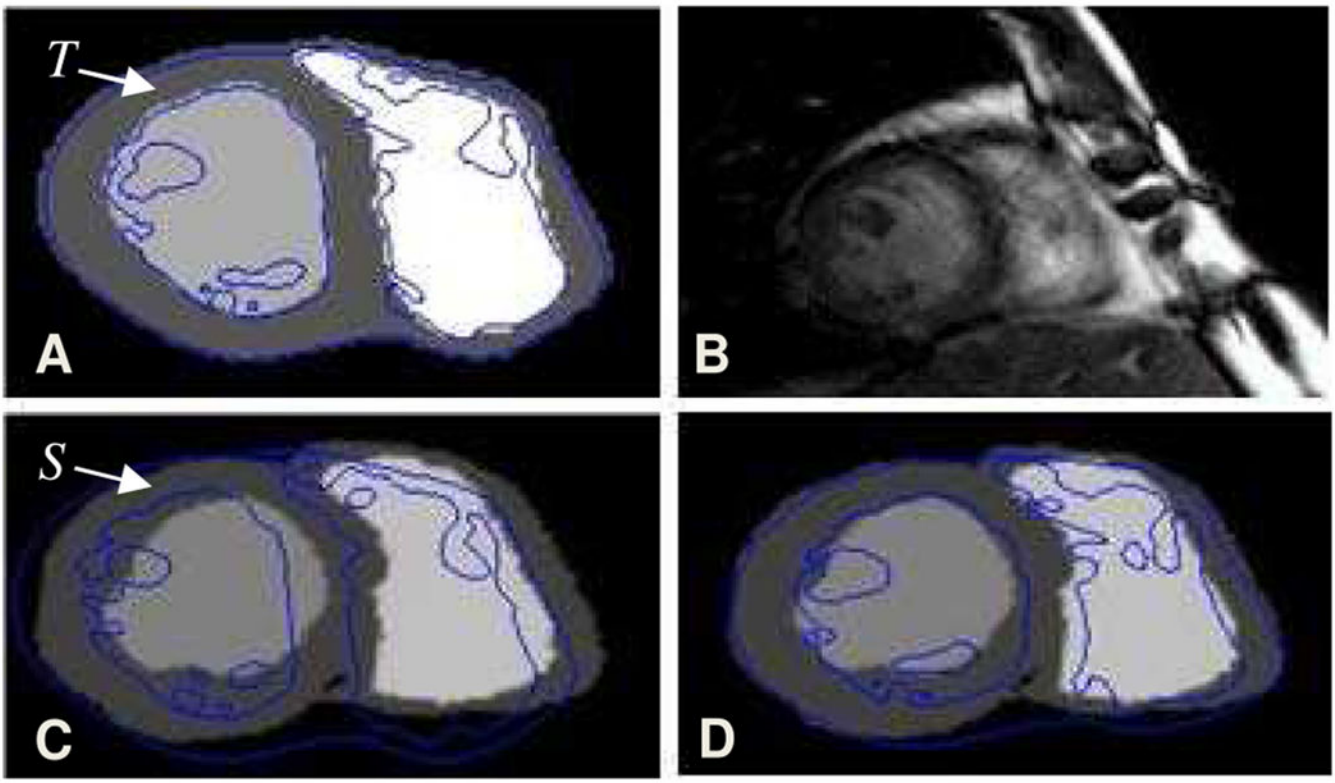

Fig. 5.

Registering the aligned LHM mesh to the given patient segmented MRI target image by hyperelastic warping. (A) The aligned FE model of the LHM voxelized at the same resolution and intensities equalized with the corresponding segmented MRI. In blue is the segmented version of the original LHM including papillary muscles outlined. This represents the starting model corresponding to the template image T for the warping analysis. (B) The mid-diastolic patient MRI image S is segmented and shown in (C) with the blue outline of the original LHM FE model. This patient image represents the target image S of the hyperelastic warping analysis. From the blue outline of the LHM, it can be seen how the LHM template image T differs from the patient target S. (D) Following completion of the warping analysis, the FE mesh boundary in blue shows the registration with the segmented target image boundary.

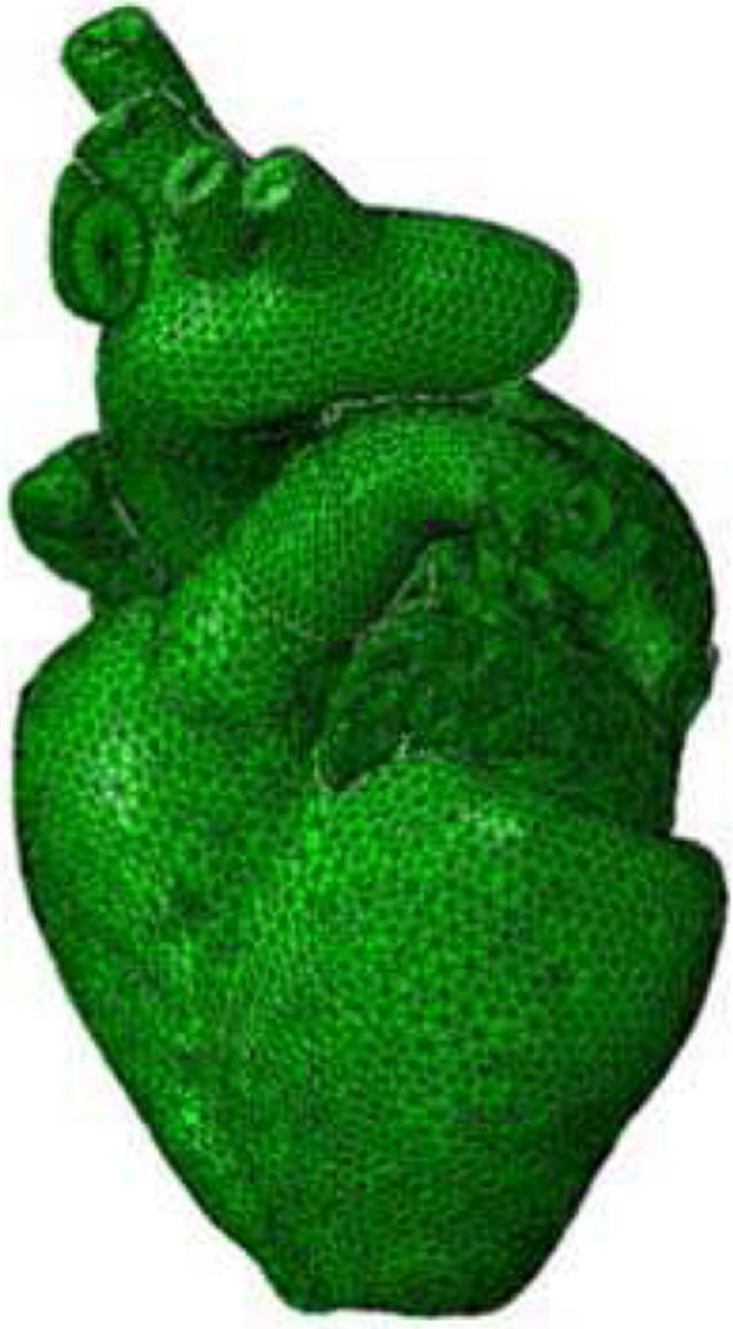

Fig. 6.
The LHM mesh, warped to match the patient MRI data, in a format that can be analyzed using Abaqus.

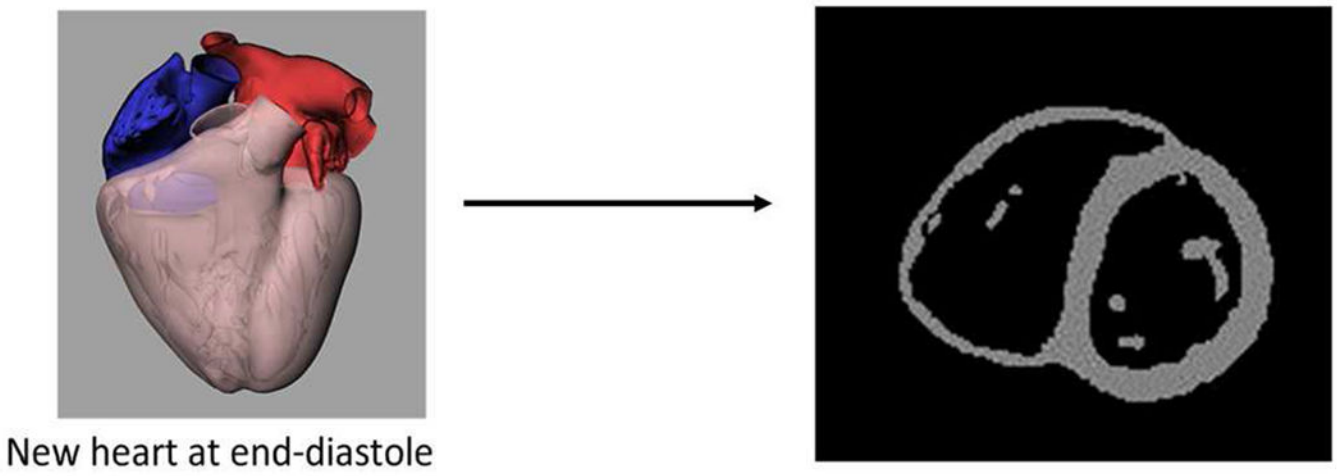

Fig. 7.
The patient specific FE model is transformed back into MRI format.

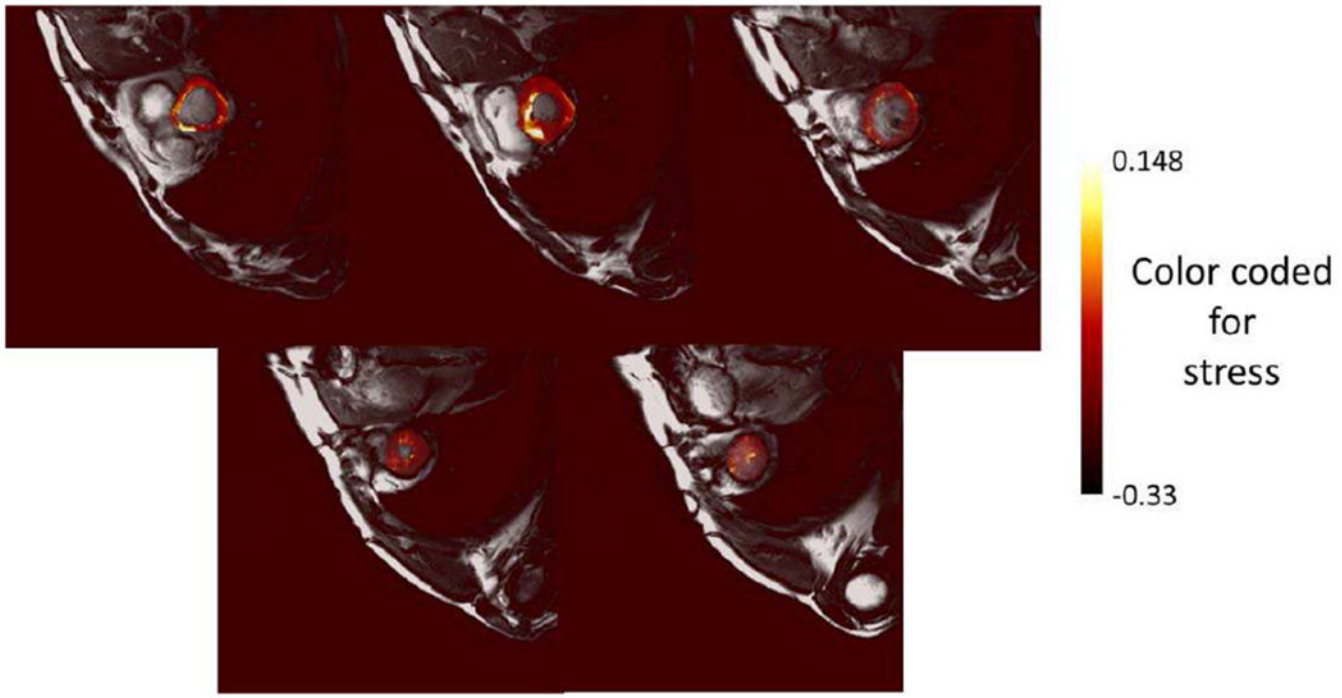

Fig. 8.

Five slices in MRI format color coded for stress (MPa). Note: 1 megapascal [MPa] = 1 newton/millimeter^2 [N/mm^2].

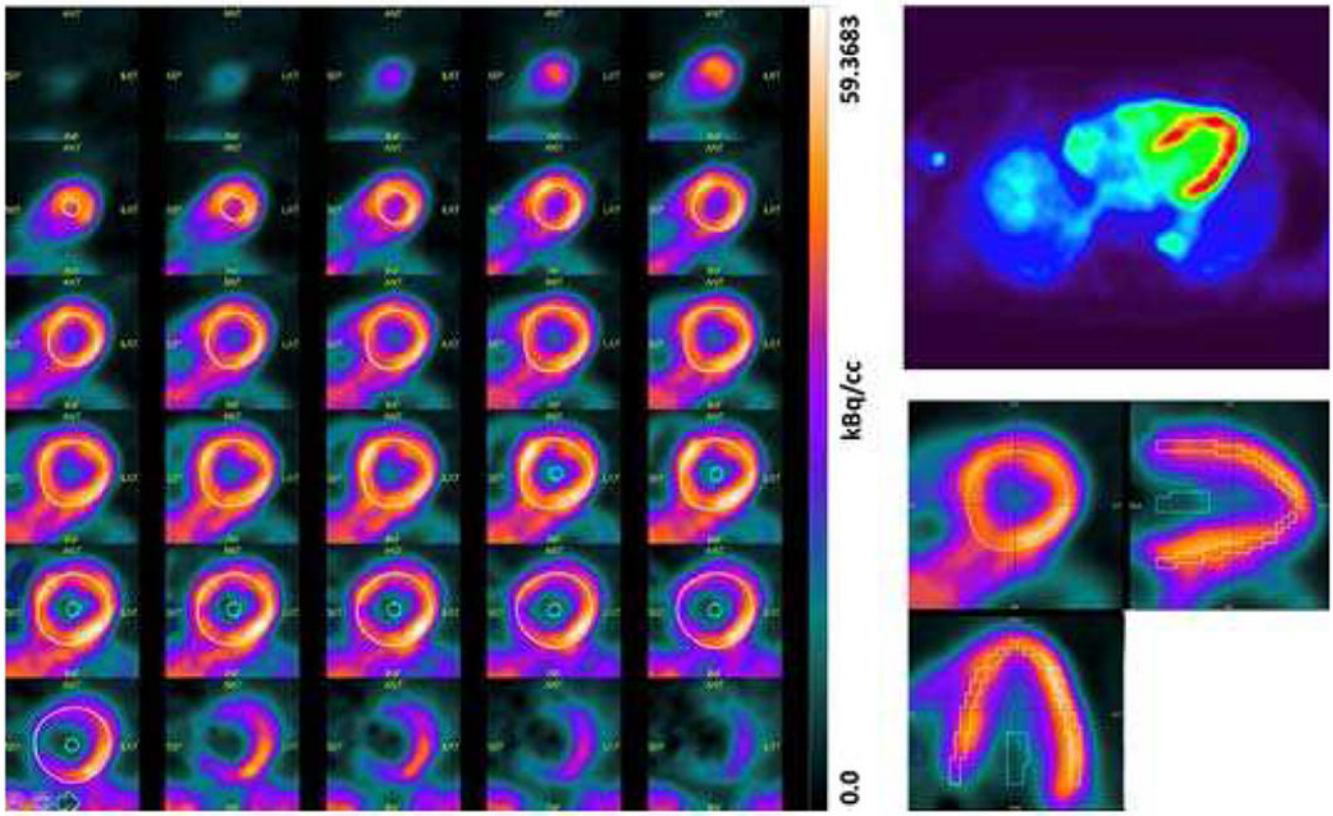

Fig. 9.

Time-of-flight reconstructed images of ^{11}C-acetate uptake in the patient heart in short axis views from apex to base (left) and transaxial (upper right) and three orthogonal views: short axis, vertical long axis, and horizontal long axis (lower right). (128 × 128 × 128 voxels of 2.7 mm).

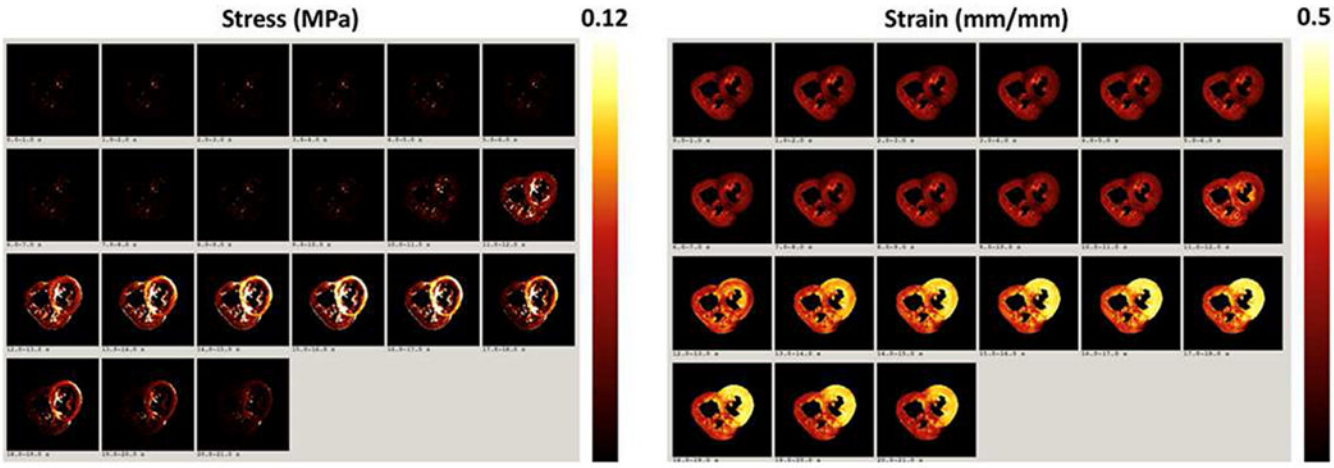

Fig. 10.

Temporal changes of the major principal component of stress (left) and absolute value of the minor principal component of strain (right) in 21 equally spaced time frames of mid cardiac slices from diastole to end-systole. (Six 1.6 mm slices of 512 × 512 pixels of 0.7 × 0.7 mm).

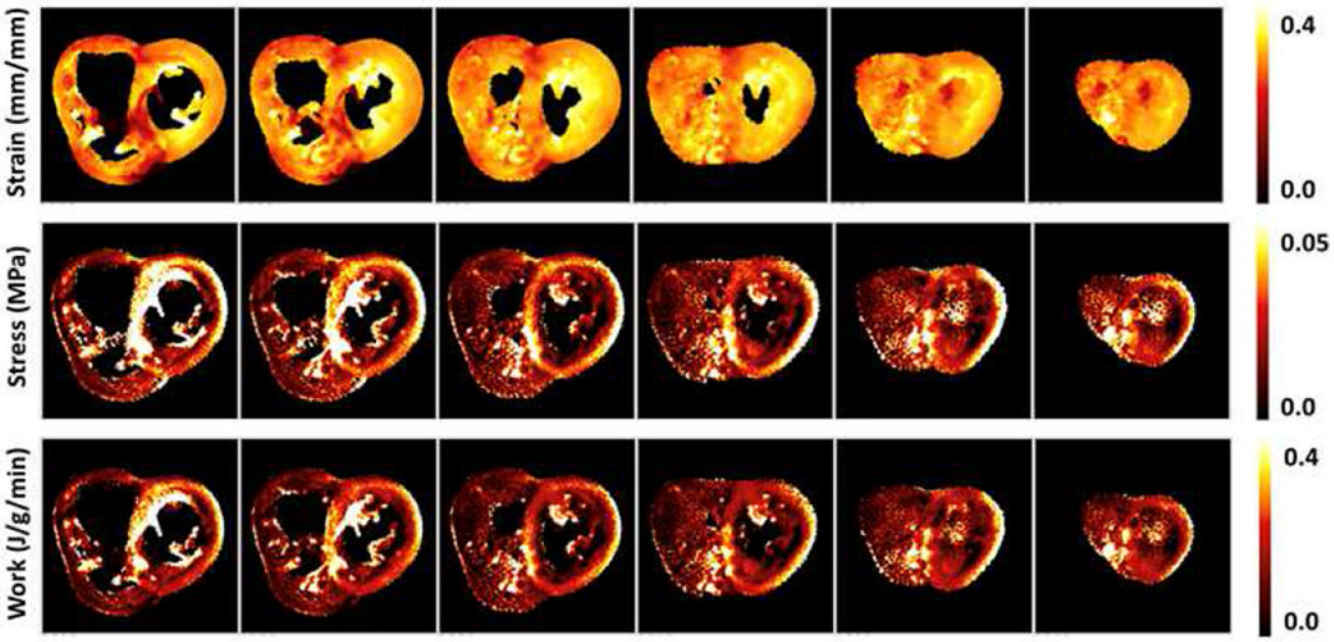

Fig. 11.

Strain, stress and *MEMW* averaged over time from end-diastole to end-systole. Six central slices of the MRI cine data provided measures of strains and stresses for the cardiac efficiency estimates. (Six 1.6 cm slices of 512 × 512 pixels of 0.7 × 0.7 mm).

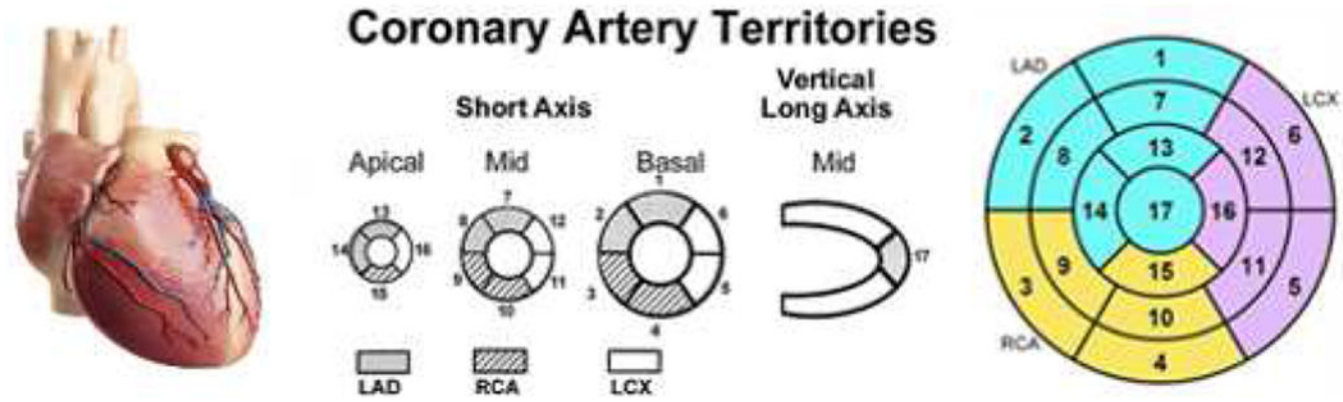

Fig. 12.

The regional myocardial segmentation based on the AHA guideline. Left: Heart ordinated with the long axis pointing downward. Center: Coronary territories with AHA 17 segments identified. (Reprinted from Manuel D. Cerqueira. Circulation. Standardized Myocardial Segmentation and Nomenclature for Tomographic Imaging of the Heart. Volume: 105, Issue: 4, Pages: 539-542, 2002. DOI: (10.1161/hc0402.). Right: Bull's-Eye plot of the AHA 17 segments.

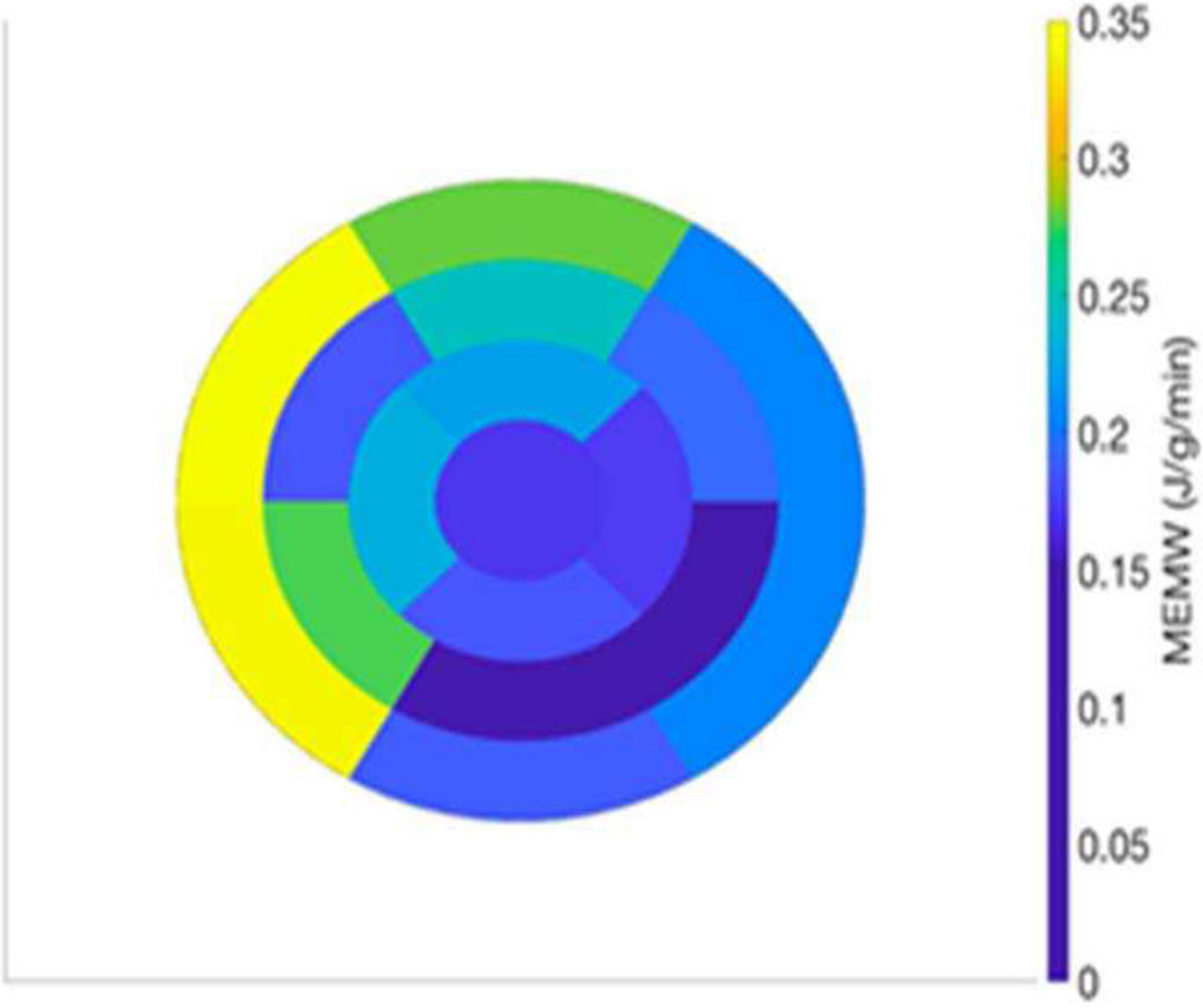

Fig. 13.

The regional myocardial equivalent minute work (*MEMW*). The regions are based on the AHA guideline (Fig. 12).

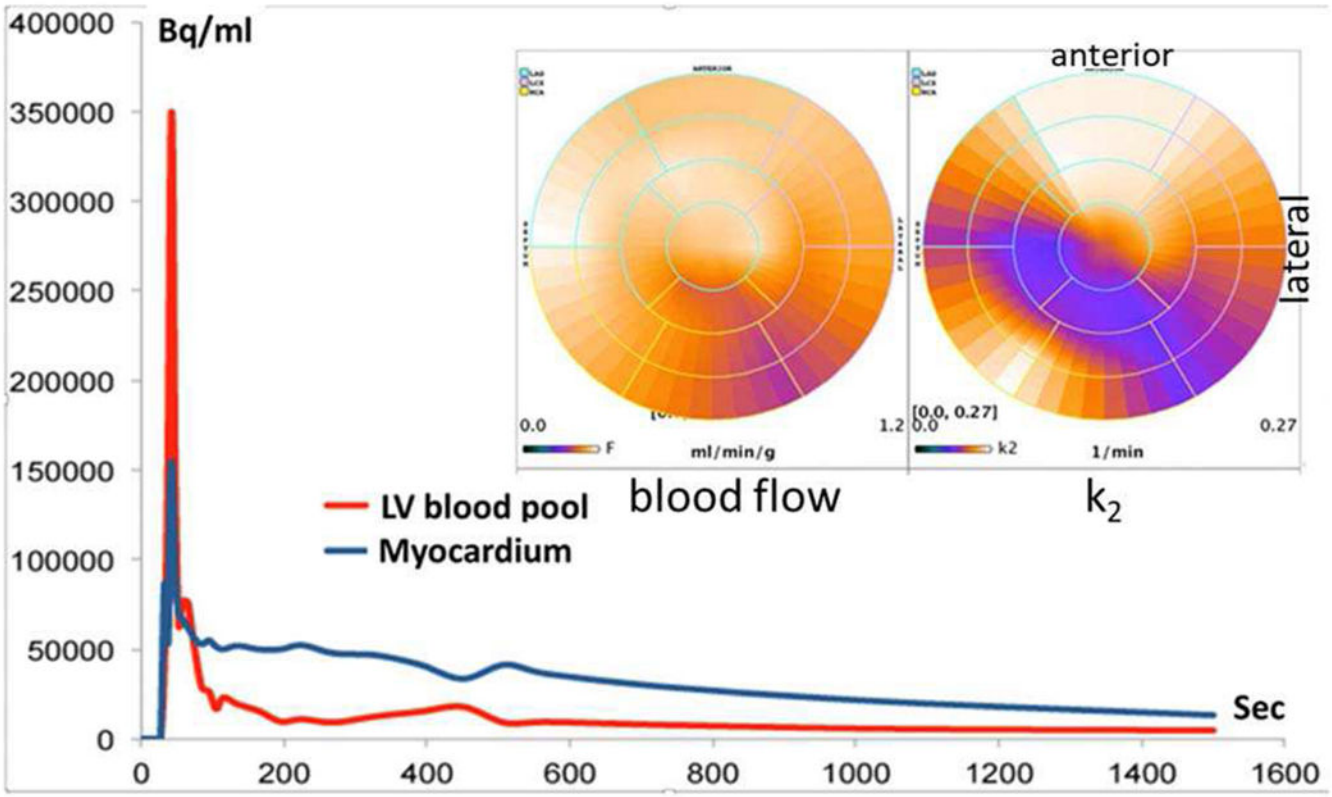

Fig. 14.

Processing dynamic PET data using ^{11}C-acetate. A 1-tissue compartment model was used to estimate blood flow and wash-out rate (k_2) of $^{11}CO_2$ from the blood. The blood and global myocardium tissue TAC is shown for 25 minutes of acquisition. The blood flow is fairly uniform in the bull's eye plot, whereas the wash-out rate k_2 in the inferior lateral wall through the apex up to the mid septal wall shows decrease indicative of reduced oxygen utilization.

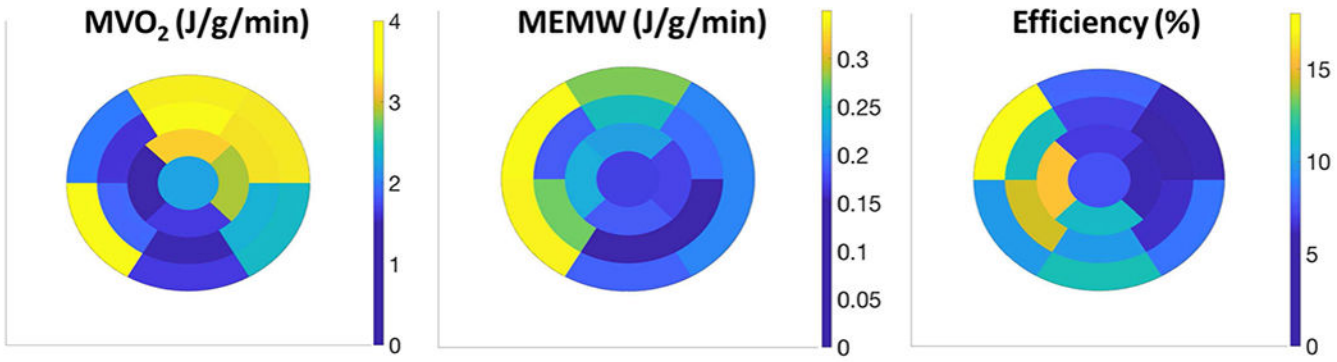

Fig. 15.

MVO_2, *MEMW*, and Efficiency shown in bull's eye format.

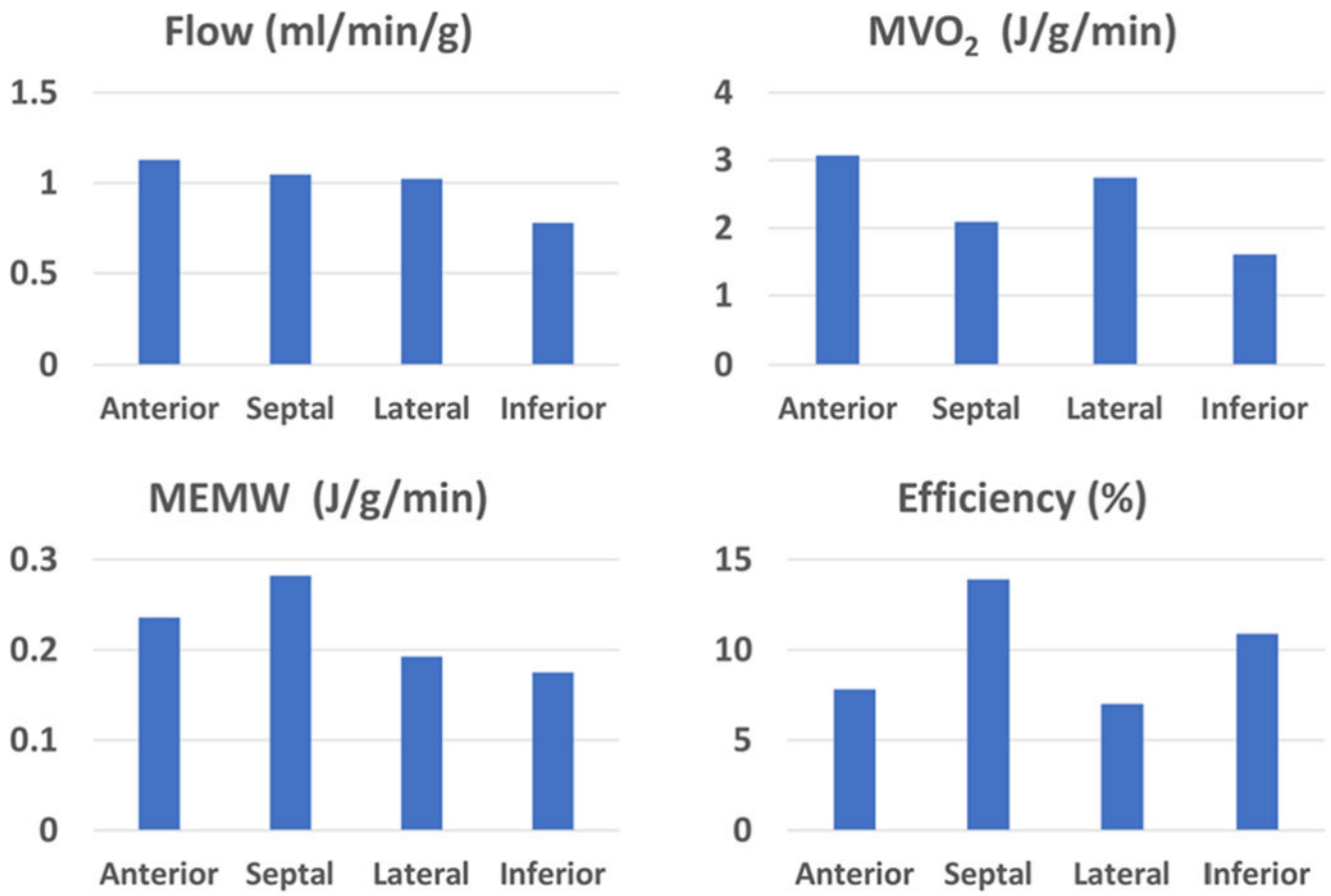

Fig. 16.

MBF, MVO_2, *MEMW*, and Efficiency in four sectors of the myocardium. The septal wall has higher efficiency compared to the lateral wall.

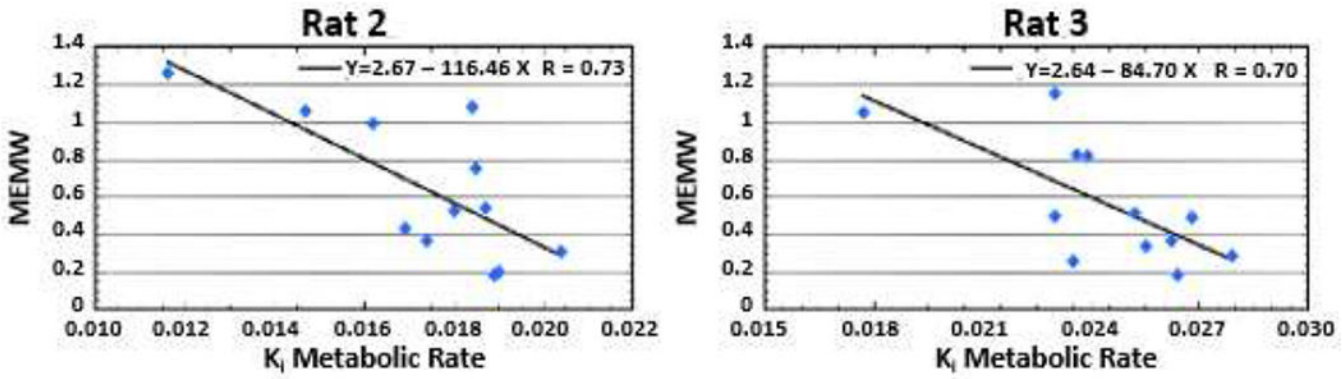

Fig. 17.

Correlation of Regional Metabolic Rate K_i of ^{18}fluorodeoxyglucose (^{18}FDG) with *MEMW*. Comparison of the mid-ventricular values of *MEMW* and the K_i values for two healthy Lewis rats showed negative correlations. These were significantly different than zero with p-values of 0.0068, and 0.0107, respectively. The heart prefers substrates that maximize efficiency such as FAs, which provide 9 kcal/gram compared to 4 kcal/gram for glucose. (Data acquired in collaboration with H.F. Wehrl and B.J. Pichler at University of Tübingen).